

Thesis

Ekaterina Avdeeva

University of Nebraska-Lincoln, USA

January 17, 2017

Abstract

This paper reviews

Contents

8	1	Introduction	2
9	1.1	Fundamental Particles and Interactions	3
10	1.2	Electroweak Interactions	5
11	1.3	Strong Interactions	8
12	1.4	Physics of Proton-Proton Collisions	9
13	1.5	Open Questions of the Standard Model	11
14	2	$W\gamma$ Production Theory and Former Experimental Results	12
15	2.1	Electroweak Theory of the Standard Model	13
16	2.2	Cross Section and Luminosity	18
17	2.3	Standard Model $W\gamma$ Production	20
18	2.4	Anomalous $W\gamma$ Production	23
19	2.5	A brief history of $W\gamma$ measurements	25
20	3	Experimental Setup	28
21	3.1	Large Hadron Collider	29
22	3.2	Compact Muon Solenoid	32
23	3.2.1	Introduction	32
24	3.2.2	Magnet	33
25	3.2.3	Tracking System	34
26	3.2.4	Electromagnetic Calorimeter	34
27	3.2.5	Hadron Calorimeter	35
28	3.2.6	Muon System	35
29	3.2.7	Triggering and Data Aquisition	36
30	3.2.8	Particle Flow Algorithm of Event Reconstruction	37
31	4	CMS Tracker Alignment	39
32	4.1	Algorithm	40
33	4.2	Selected Results	45
34	5	$W\gamma$ Cross Section Measurement	46

35 1 Introduction

36 Elementary particle physics describes fundamental particles and their interactions. Fundamental
37 particles are the smallest constituents of our Universe. When examined at smaller scales, the
38 substances around us consist of molecules, molecules consist of atoms. In an atom there is a
39 nucleus made of neutrons and protons and some number of electrons occupying orbits around
40 the nucleus. Protons and neutrons have a structure while an electron is not known to have any
41 internal structure, therefore, an electron is an example of a particle which is considered to be
42 fundamental.

43

44 Interactions of elementary particles are described by quantum field theories which incorporate
45 principles of the quantum mechanics and the special theory of relativity. The set of such theories,
46 including quantum elecrtrodynamics (QED), quantum chromodynamics (QCD) and the theory
47 of weak interactions is called the Standard Model (SM). Current observations have proved the
48 SM to be an accurate description of elementary particle interactions.

49

50 However, there are several experimental observations that are not described by the SM such
51 as effects of gravity, dark matter, dark energy, matter/antimatter asymmetry and others. There-
52 fore, the SM is not a complete theory of particle interactions. There are several SM extensions
53 offered by theorists as well as radically new theories waiting for experimental confirmation or
54 exclusion.

55

56 Some SM extensions and new theories predict the existence of heavy particles with masses
57 lying beyond experimentally reachable energies. The search of these particles is a priority in
58 particle physics. One source of highly energetic elementary particles is cosmic rays. The most
59 energetic particles ever observed came from this source. However, cosmic rays are totally uncon-
60 trollable and such highly energetic particles are rare. If we want to produce a large number of
61 particles in a given energy range, we need to use a particle accelerator. A large amount of data
62 allows experimentalists to perform a statistical analysis and increase the probability of finding a
63 new particle if it exists.

64

65 Symmetric colliding beams is the most effective way to produce as heavy particles as possible
66 given the energies of the colliding particles. Compared to experiments colliding a single beam at
67 a fixed target, in the case of a symmetric collision the total momentum of two colliding particles
68 is zero and, therefore, much larger fraction of energy can transfer to a mass of a new particle.
69 The Large Hadron Collider (LHC) is one such collider with the highest energy in the world. It
70 can produce the most massive particles to probe physics beyond the SM (BSM).

71

72 The Compact Muon Solenoid (CMS) is one of two general-purpose detectors at the LHC. It
73 is placed at one of four collision points. CMS has a broad physics program including searches for
74 the BSM physics as well as the precision measurements of the parameters of the SM itself. The
75 measurement of this dissertation is a SM measurement with CMS data collected in 2012 in pp
76 collisions of LHC with beam energies of 4 TeV. The result can be compared to the SM prediction.
77 Certain BSM theories predict a deviation of the result of this measurement from its SM value,
78 therefore, with this measurement, in addition to testing the SM, we also search for a new physics.

79

80 The rest of this chapter gives general introductory information about the SM while Ch. 2
81 concentrates on the theory of the SM and BSM $W\gamma$ production and also discusses previous
82 measurements of this process. Chapter 3 describes LHC and CMS in more details. Chapter 4
83 explains one specific detail of the CMS operation that is the spacial alignment of the tracking
84 detector of charged particles. Finally, Ch. 5 describes the details of the measurement of this
85 dissertation and reports the results.

86

87 1.1 Fundamental Particles and Interactions

88 The SM describes interactions of elementary particles. There are four fundamental interactions:
89 electromagnetic, strong, weak and gravitational. The gravity is not included into the SM but its
90 effect on particles is negligible compared to the other forces which makes it possible to develop a
91 theory of the particle physics and conduct experiments even without having the gravity included
92 into the model.

93
94 All fundamental elementary particles in the SM can be split into three categories by their
95 spins. There are fermions which possess spin $s=1/2$, there are gauge bosons which are vector
96 particles ($s=1$) and there is the Higgs boson which is a scalar particle ($s=0$).

97
98 The fermions are arranged into three generations, each generation consists of a quark with
99 charge $Q=+2/3$ (up, charm, and top quarks), a quark with $Q=-1/3$ (down, strange, and bottom
100 quarks), a charged lepton with $Q=-1$ (electron, muon, and tau-lepton) and a neutrino (electron,
101 muon, and tau neutrinos) which is electrically neutral. Each quark can carry any of three colors:
102 red, blue, or green. Additionally, each fermion has its antiparticle. Therefore, the total number
103 of fundamental fermions is $(6(\text{leptons}) + 6(\text{quarks}) \cdot 3(\text{colors})) \cdot 2(\text{to include antiparticles}) = 48$.

104
105 Corresponding particles in different generations have the same charges, spins and interaction
106 properties but masses of particles increase with generation. These mass differences lead
107 to different decay properties because a particle A can decay to particles B and C only if their
108 masses relate as $m_A > m_B + m_C$. Thus, an electron is a stable particle, a muon decays as
109 $\mu^- \rightarrow e^- + \bar{\nu}_e + \nu_\mu$, a tau-lepton, as the heaviest charged lepton, has the largest number of decay
110 channels amongst the charged leptons: $\tau^- \rightarrow \mu^- + \bar{\nu}_\mu + \nu_\tau$, $\tau^- \rightarrow e^- + \bar{\nu}_e + \nu_\tau$, $\tau^- \rightarrow \nu_\tau + \text{quarks}$.

111
112 In addition to fermions, the SM includes gauge bosons which are interaction mediators. They
113 are called mediators because fermions interact with each other by exchanging them. For example,
114 two charged fermions can interact with each other by exchanging a photon. Such interaction is
115 called electromagnetic interaction and a photon is a mediator for the electromagnetic interaction.
116 Similarly, a gluon is a mediator for strong interactions, and W^\pm and Z^0 bosons are mediators
117 for weak interactions. W^\pm and Z^0 bosons are massive while a photon and a gluon are massless
118 particles.

119
120 The last SM particle is the Higgs boson. The Higgs boson is a scalar neutral particle which
121 is playing a critical role in the electroweak symmetry breaking. The Higgs mechanism explains
122 how W and Z bosons become massive particles.

123
124 All the particles are summarized in Fig. 1. These and only these fundamental particles and
125 their antiparticles have been discovered by now. However, there are many composite particles
126 which are called hadrons. Hadrons can consist of three quarks (baryons), quark and antiquark
127 (meson), or three antiquarks (antibaryons). Hadrons always possess an integer charge.

128
129 Most of the particles are short-lived and decay within microseconds. The only stable particles
130 are protons and antiprotons, electrons and positrons, neutrinos and antineutrinos, photons,
131 and, in some sense, gluons. However, if a particle cannot decay, it does not mean that it would
132 live forever. There are many different kinds of reactions in which particles can disappear. An-
133 tiprotons and positrons would immediately annihilate with protons and electrons, photons can
134 be absorbed by charged particles, electrons and protons can scatter to produce neutrons and
135 neutrinos and many other reactions are possible.

136
137 In this dissertation, the study of $pp \rightarrow W\gamma + X \rightarrow l\nu\gamma$ process where $l = e, \mu$ is presented. The
138 $W\gamma$ production with leptonic W decays proceeds through one of the following three processes:
139 the initial state radiation where a photon is emitted from one of the incoming partons, the final
140 state radiation where a photon is radiated off the charged lepton from the W boson decay, and,
141 finally, the triple gauge coupling (TGC) where a photon is emitted from the W boson. Many

142 BSM theories predict an enhancement of the TGC production over the SM value and, therefore,
 143 the experimental search for such an enhancement is a good test for such theories.

144
 145 Therefore, the focus of this study is an interaction between a photon and a W boson however
 146 many other SM particles are relevant too. Thus, a charged lepton and a neutrino appear as the
 147 final state particles, a quark and an antiquark appear as initial state particles and all fundamental
 148 particles except the Higgs boson participate in various background processes. Subsequent
 149 chapters describe these particle interactions in more details.

150

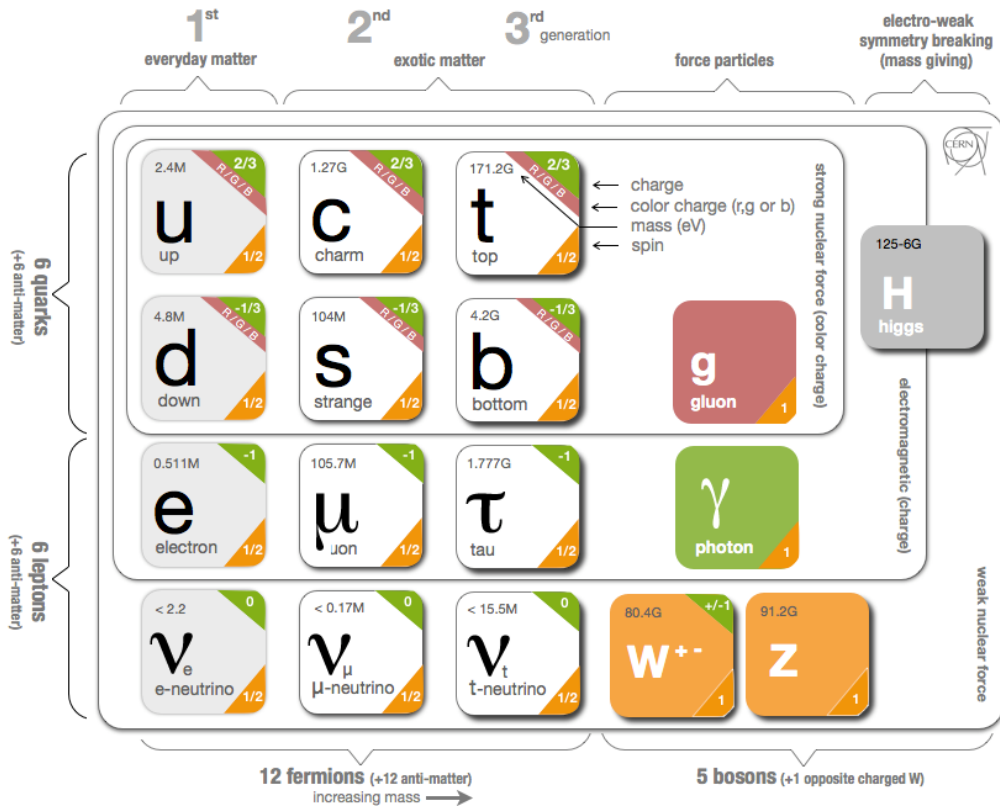


Figure 1: Standard Model Particles and Interactions. Source of the figure: [2].

1.2 Electroweak Interactions

All electrically charged particles participate in electromagnetic interactions. The theory of electromagnetic interactions is called quantum electrodynamics (QED). All electromagnetic interactions are mediated by a photon, a spin-one electrically neutral massless particle, and can be reduced to one elementary process (Fig. 2, left). This process represents a charged fermion radiating or absorbing a photon. Such elementary process itself is forbidden by the energy conservation law but this element is a base of an actual process. For example, the Bhabha scattering, $e^+e^- \rightarrow e^+e^-$, occurs through e^+e^- annihilation with further production of a new e^+e^- pair (Fig. 2, middle) or through exchange of a photon between the positron and the electron (Fig. 2, right). Both cases involve nothing except the electromagnetic elementary process (Fig. 2, left). Such graphical representations of the particle physics processes are called Feynman diagrams.

162

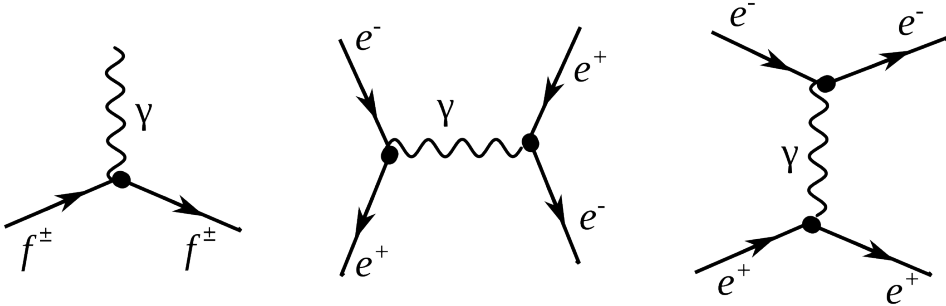


Figure 2: Electromagnetic interactions. Left: a photon radiation off a charged fermion, middle and right: Bhabha scattering.

As for the weak interactions, there are two kinds of them: neutral (mediated by a Z boson) and charged (mediated by a W^\pm boson). Elementary processes with W and Z bosons are shown in Fig. 3. Because the electric charge must be conserved at any vertex, a particle radiating or absorbing a W boson converts to a different particle. Thus, a charged lepton converts to a neutrino (or vice versa) as shown in Fig. 3, top middle. Each lepton carries a lepton flavor number (Tab. 1). Lepton flavor is conserved in any interaction, thus an electron radiating a W boson always converts to an electron neutrino, a muon converts to a muon neutrino etc.

170

Table 1: Lepton Flavor Number

particles	L_e	L_μ	L_τ
e^-, ν_e	+1	0	0
$e^+, \bar{\nu}_e$	-1	0	0
μ^-, ν_μ	0	+1	0
$\mu^+, \bar{\nu}_\mu$	0	-1	0
τ^-, ν_τ	0	0	+1
$\tau^+, \bar{\nu}_\tau$	0	0	-1

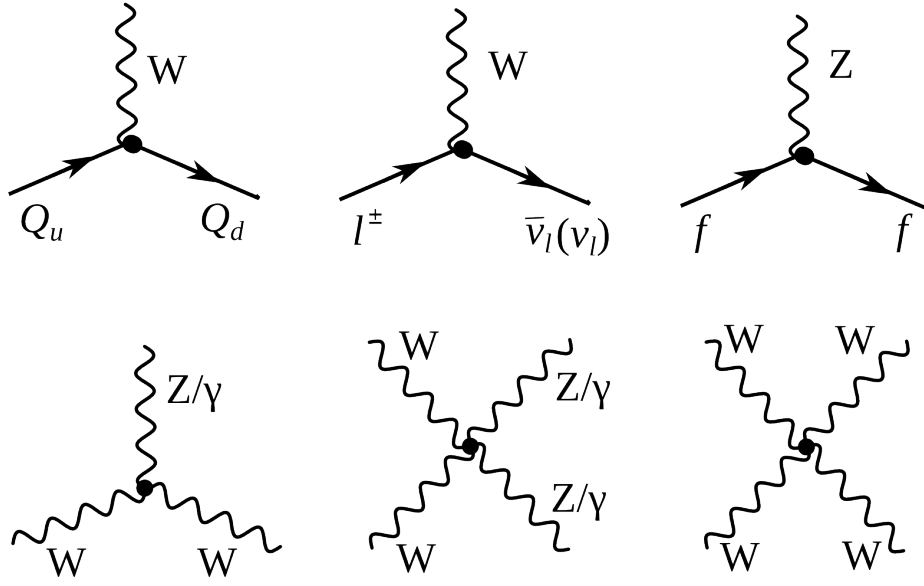


Figure 3: Weak elementary processes and gauge couplings. Top left: a quark with charge $Q=+2/3$ enters, emits a W boson, and a quark with charge $Q=-1/3$ escapes. Top middle: a charged lepton enters, emits a W boson, and a neutrino or antineutrino escapes conserving a lepton flavor number. Top right: a fermion enters, emits a Z boson and escapes. Bottom left: TGC couplings $WW\gamma$ and WWZ . Bottom middle: QGC couplings $WW\gamma\gamma$, $WWZ\gamma$ and $WWZZ$. Bottom right: QGC coupling $WWWW$.

From top left diagram in Fig. 3 we see that if a quark with $Q=+2/3$ enters, then a quark with $Q=-1/3$ escapes and, therefore, the flavor of the quark is changed. The charged weak interaction is the only interaction which changes a quark flavor. The probability of each of three quarks with $Q=-1/3$ to be born is determined by the Cabibbo-Kobayashi-Maskawa matrix which relates mass eigenstates d , c and b to weak eigenstates d' , c' and b' (Eq. 1). Absolute values of the matrix elements are all known (Eq. 2) and are the highest for the quark of the same generation as the initial state quark. In the particular case shown in the top left diagram in Fig. 3, u is the initial state quark and d has the highest probability to be produced after an interaction with a W boson but s and b can also be produced if there is enough energy.

180

$$\begin{pmatrix} d' \\ s' \\ b' \end{pmatrix} = \begin{pmatrix} V_{ud} & V_{us} & V_{ub} \\ V_{cd} & V_{cs} & V_{cb} \\ V_{td} & V_{ts} & V_{tb} \end{pmatrix} \begin{pmatrix} d \\ s \\ b \end{pmatrix} \quad (1)$$

$$\begin{pmatrix} |V_{ud}| & |V_{us}| & |V_{ub}| \\ |V_{cd}| & |V_{cs}| & |V_{cb}| \\ |V_{td}| & |V_{ts}| & |V_{tb}| \end{pmatrix} = \begin{pmatrix} 0.97 & 0.23 & 0.00 \\ 0.23 & 0.97 & 0.04 \\ 0.01 & 0.04 & 1.00 \end{pmatrix} \quad (2)$$

An elementary process of a neutral weak interaction is an emission a Z boson off a fermion line (right top diagram in Fig. 3). Diagrams with a Z boson are very similar to ones with a photon except a photon can only be radiated off a charged particle but a Z boson can also be radiated off a neutrino or antineutrino.

185

186 The bottom diagrams in Fig. 3 are gauge bosons coupling diagrams including self-coupling
 187 of a W boson, its interaction with a Z boson and its electromagnetic radiation of a photon.
 188 Charge-conserving TGC and quartic gauge couplings (QGC) containing two or four W bosons
 189 are all possible in the SM: WWZ , $WW\gamma$, $WWZZ$, $WWZ\gamma$, $WW\gamma\gamma$, and $WWWW$.
 190

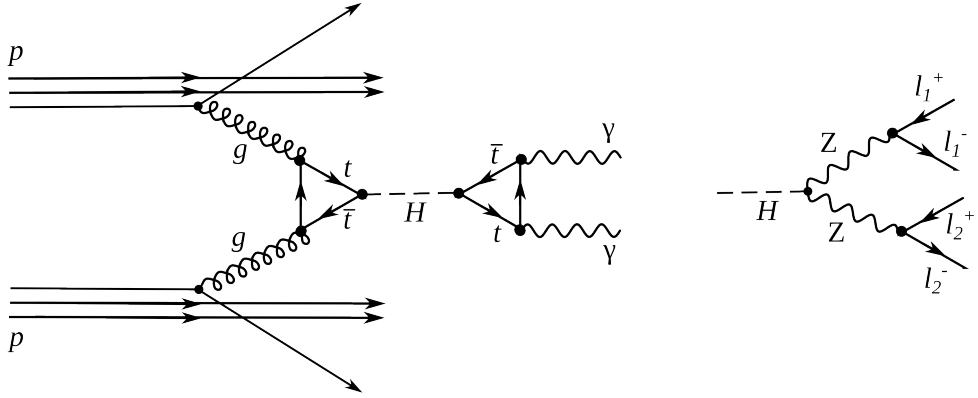


Figure 4: The Higgs boson production and decay. Left: $H \rightarrow \gamma\gamma$, right: $H \rightarrow ZZ \rightarrow 4l$.

191 Electromagnetic and weak interactions are unified by the electroweak Glashow-Weinberg-
 192 Salam (GWS) theory which is based on $SU(2) \times U(1)$ symmetry. $SU(2)$ is the symmetry of
 193 weak isospin which generates three bosons: W^1 , W^2 and W^3 . $U(1)$ is the symmetry of the weak
 194 hypercharge and generate one neutral boson B . W^1 and W^2 are mixed to create W^+ and W^-
 195 mediators while W^3 and B are mixed to create a Z boson and a photon. Therefore, the GWS
 196 theory considers electromagnetic and weak forces as different manifestations of the electroweak
 197 force. The electroweak theory is discussed in greater details in Ch. 2.

198 Weak interactions are mediated by heavy bosons ($M_W = 80$ GeV, $M_Z = 91$ GeV) while
 199 electromagnetic interactions are mediated by a massless photon, thus, the electroweak symmetry
 200 is broken. To explain this phenomenon, the Higgs mechanism was introduced. The mechanism
 201 predicted an existence of an additional boson: the Higgs boson. The Higgs boson was a missing
 202 piece of the SM for many years and was finally discovered in 2012 at LHC by ATLAS and CMS
 203 collaborations through the processes shown in Fig. 4 [3], [4].

205 The measurement in this dissertation is an electroweak measurement because the process
 206 involves a W boson. It includes an interaction of a W boson with leptons and quarks as well as
 207 the TGC $WW\gamma$. Thus, the measurement is a good test of the SM electroweak theory.
 208

209

²¹⁰ **1.3 Strong Interactions**

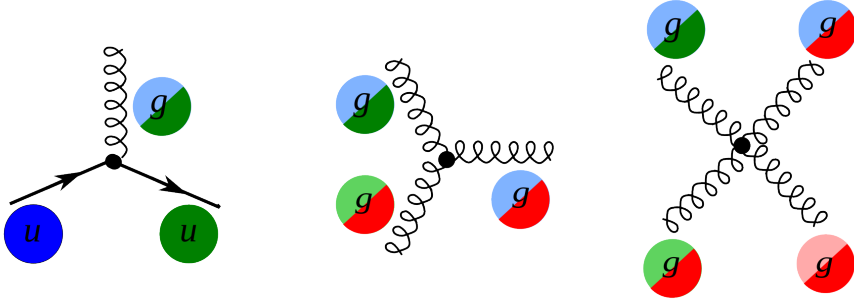


Figure 5: Elementary processes of strong interactions

²¹¹ The third fundamental force after the electromagnetic and weak ones is the strong force. The
²¹² strong force is responsible for gluing protons and neutrons together in the nuclei as well as for
²¹³ forming protons and neutrons themselves. The strong interactions occur by exchanging gluons
²¹⁴ which are spin-one massless electrically neutral particles.

²¹⁵
²¹⁶ The elementary strong processes are shown in Fig. 5. There are three elementary processes:
²¹⁷ qqg , ggg and $gggg$, all are involving particles with color charges. Thus, gluons couple to quarks
²¹⁸ and self-couple. Color charges must be conserved at each elementary process of the strong inter-
²¹⁹ action. Each quark possesses one of three colors at a time, and there are eight types of gluons
²²⁰ to cover all possible color exchanges.

²²¹
²²² The coupling constant of the strong interaction depends on the distance between interacting
²²³ particles: it becomes larger as the distance becomes larger and smaller as the distance becomes
²²⁴ smaller. As the distance approaches zero, the coupling constant approaches zero too, and, thus,
²²⁵ in the asymptotic limit two quarks located at the same place do not interact. This property is
²²⁶ called asymptotic freedom.

²²⁷
²²⁸ On the other hand, when the distance between quarks becomes larger, the coupling constant
²²⁹ also becomes larger. This property confines quarks to always stay in the color neutral combi-
²³⁰ nations (hadrons), it forbids the existence of free quarks. A combination becomes color neutral
²³¹ when there is the same amount of color and anticolor or if there is the same amount of each of
²³² the three colors. Thus, mesons are comprised of a quark and an antiquark with the opposite
²³³ color charges, and baryons are composed of three quarks: red, green and blue one. Examples of
²³⁴ baryons include such well-known particles as a proton and a neutron.

²³⁵
²³⁶ The asymptotic freedom and the confinement are properties that are specific to strong inter-
²³⁷ actions. The theory of strong interactions is called the quantum chromodynamics (QCD)
²³⁸ which is a quantum field theory invariant under $SU(3)$ color transformations. When the cou-
²³⁹ pling constant is much less than one $\alpha_s \ll 1$, the perturbative approach can be used to compute
²⁴⁰ observables.

²⁴¹
²⁴² The $W\gamma$ process being measured in this dissertation is not intended to test QCD, but a good
²⁴³ understanding of QCD is essential for performing this measurement because the QCD correc-
²⁴⁴ tions to the Feynman diagrams of the process are large and have to be taken into account when
²⁴⁵ producing simulation. In addition, QCD describes the dynamics of quarks and gluons within
²⁴⁶ colliding protons and predicts probabilities of one or another quark-antiquark pair to interact.
²⁴⁷ Physics of proton-proton collisions is discussed in Ch. 1.4.

249 1.4 Physics of Proton-Proton Collisions

250 Consider a pp collision at LHC. The proton energies are so high that each proton behaves as a
 251 complex structure. A proton is a baryon, it consists of three quarks: uud . These three quarks
 252 are called valence quarks. They interact with each other by exchanging gluons which produce
 253 virtual $q\bar{q}$ pairs (Fig. 6). Such virtual quarks are also called sea quarks.
 254

255 Any parton, quark, antiquark or gluon, from one proton can interact with any parton from
 256 another proton. Probabilities $f_i(x, Q^2)$ of any particular constituent i to interact are described
 257 partially by QCD and partially by experimental measurements and depend on the momentum
 258 transfer Q and the momentum fraction of a specific parton x . These probabilities are called
 259 parton distribution functions (PDFs).
 260

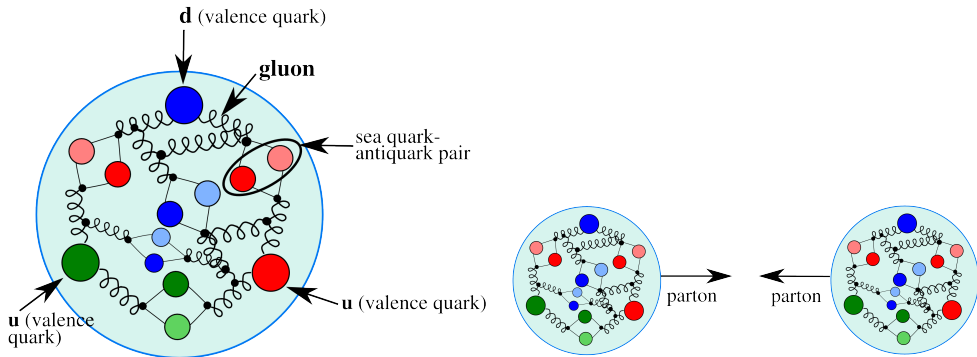


Figure 6: The proton structure (left) and the proton-proton collision (right).

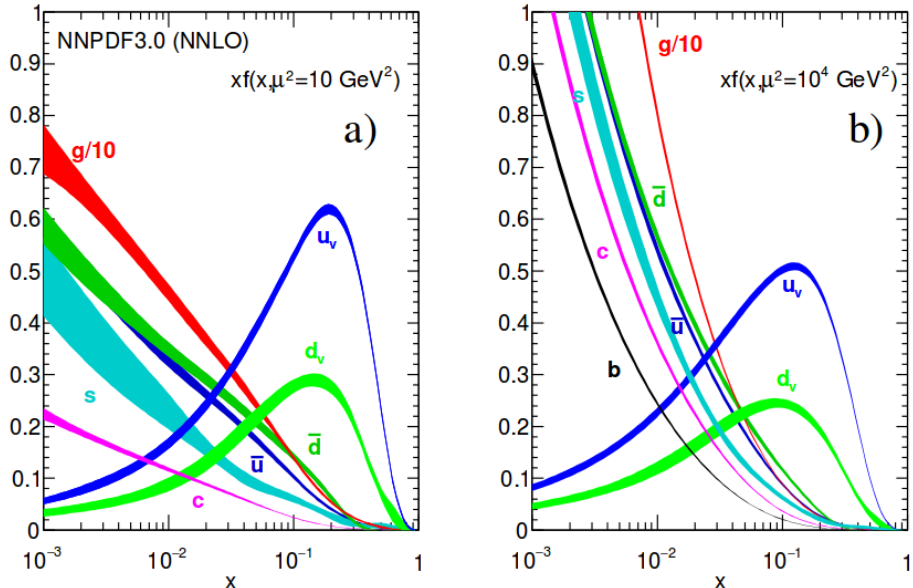


Figure 7: Parton distribution functions [5].

261 For large Q^2 and x gluon-gluon interactions have the largest probabilities to occur (Fig. 7).

262 However, gluons do not couple directly to a W boson, thus, in the $W\gamma$ measurement we are
263 mostly interested in quark-antiquark pairs which would have a total charge corresponding to the
264 charge of a W boson (± 1). Since we have u and d as valence quarks and we know that the
265 probability to couple to the same generation quark in charged weak interactions is the highest,
266 most of the W bosons are created by $u\bar{d}$ and $d\bar{u}$ pairs however other $q\bar{q}'$ combinations with the
267 total charges of ± 1 are also possible. As we look for events containing $W\gamma$ we also have other
268 events mimicking our process. Such background events can be produced by any pair of partons.

269

270 1.5 Open Questions of the Standard Model

271 While the SM is an accurate description of all particle physics experimental results, there are
272 certain phenomena which are not included into the SM. In this subsection we discuss some of
273 them.

274 The gravitational interactions do not fit into the SM. It is the open question whether the
275 quantum theory of gravity is possible and whether there is a mediator of the gravitational in-
276 teractions. Also, it is not known why the gravitational force is so much weaker than the other
277 forces. One possible explanation comes from a theory which predicts extra spatial dimensions
278 beyond the three we experience (e.g. the string theory). In this case, it is possible that the
279 gravitational force is shared with other dimensions and only a fraction is available in our three
280 dimensions.
281

282 Another mystery of the universe is its composition: it is known from the studies of the grav-
283 itational effects that our universe consists of dark energy by 68%, of dark matter by 27% and of
284 baryon matter only by 5% [6]. The dark energy resists the gravitational attraction and acceler-
285 ates the expansion of the universe, and is not detectable by any effects except gravitational. The
286 understanding of dark energy is a question of general relativity rather than particle physics. The
287 dark matter, however, likely consists of particles and therefore is a subject of particle physics.
288 It does not radiate and that is why it cannot be detected by telescopes. The nature of the dark
289 matter is not known but its constituents must be very stable to remain since the Big Bang. The
290 theory of the supersymmetry which is unifying fundamental particles and mediators predicts
291 many of new heavy particles and the lightest supersymmetric particle, the neutralino, is a good
292 candidate for dark matter.
293

294 One more open question is the reason for the matter/antimatter asymmetry. Matter and
295 antimatter should have been created in the same amount at the moment of the Big Bang. Most
296 of it has annihilated but because of asymmetry, there was more matter than antimatter which
297 led to the state of the Universe we observe now. There is a phenomenon of the CP-violation
298 in weak interactions observed and described which predicts the asymmetry at a certain level.
299 However, the effect of the CP-violation is not large enough to account for the observed amount
300 of the matter and, therefore, the total matter/antimatter asymmetry remains unexplained.
301

302 The measurement of the photon transverse momentum spectrum (P_T^γ) of the $W\gamma$ process has
303 a goal to both test the SM and search for the BSM physics. The low P_T^γ region is not expected
304 to be affected by any new physics and must agree well with the SM predictions while the high
305 P_T^γ region may indicate an existence of new physics if there is an enhancement over the SM
306 predictions. The excess would be indirect evidence of the BSM particles like supersymmetric
307 particles or additional gauge bosons which could be part of the explanation of the dark matter
308 presence or difference in magnitudes of different interactions. More theoretical details about the
309 SM description of $W\gamma$ process as well as possible BSM physics are given in Ch. 2.
310

312 2 $W\gamma$ Production Theory and Former Experimental Re- 313 sults

314 Chapter 2 provides deeper theoretical background for the measurement of this dissertation and
315 discusses former experimental results. The derivation of the electroweak Lagrangian is described
316 in Ch. 2.1, including the appearance of triple gauge coupling (TGC) and quartic gauge coupling
317 (QGC) terms. Then concepts of the cross section and the luminosity are discussed in Ch. 2.2.
318 More specific details regarding the SM cross section of $W\gamma$ are summarized in Ch. 2.3. Possi-
319 ble causes and potential effects of anomalous TGC (aTGC) are explained in Ch. 2.4. Finally,
320 Ch. 2.5 lists former physics experiments which probed the same aTGC vertex which is probed
321 in the measurement of this dissertation including measurements of exactly the same process at
322 lower LHC beam energy.

323

324 2.1 Electroweak Theory of the Standard Model

325 To develop a quantum field theory, we start with the Lagrangian of free fermions. In order to
326 describe a system with a conserved physical quantity, the Lagrangian is required to satisfy a
327 local invariance with respect to a certain transformation. For instance, a conservation of electric
328 charge requires local invariance under $U(1)$ transformation for the QED Lagrangian [7]. The re-
329 quirement of local invariance introduces an interaction between one or more new vector fields and
330 our free fermions. The new vector fields are mediators of an interaction conserving the physical
331 quantity. To provide a full description for a new boson field, in addition to the interaction term
332 we introduce an invariant term for the kinetic energy of the boson. Such an approach allows us
333 to derive a Lagrangian which is locally invariant with respect to a certain gauge transformation
334 and contains interacting fermions as well as interaction mediators.

335 The SM is a quantum field theory invariant under the local $SU(3)_C \times SU(2)_L \times U(1)_Y$ trans-
336 formation [7]. The SM Lagrangian includes all observed quantum fields and their interactions.

337 The part of the SM Lagrangian based on the $SU(3)_C$ symmetry is called QCD or the theory
338 of strong interactions. QCD has three types of charges which are called colors: red, blue, and
339 green. To be a subject of the strong interaction, a fermion must posses a color charge. Quarks
340 and antiquarks are such fermions. The requirement to satisfy the gauge invariance with respect
341 to $SU(3)_C$ transformations generates eight massless gluons, and the non-abelian nature of the
342 $SU(3)$ group generates self-interactions of gluons including three-gluon and four-gluon vertices.

343 The part of the SM Lagrangian based on the $SU(2)_L \times U(1)_Y$ symmetry is the founda-
344 tion of the unified theory of electroweak interactions. $SU(2)_L$ reflects transformations in the
345 weak isospin space of left-handed fermions ([1], Ch. 9) while $U(1)_Y$ reflects transformations in a
346 weak hypercharge space of all fermions. The requirement of the local gauge invariance generates
347 four massless vector bosons which are mediators of electromagnetic and weak interactions. The
348 non-abelian structure of the $SU(2)$ group generates gauge boson self-couplings the same way as
349 self-interactions of gluons appear in QCD.

350 Mass terms for the vector bosons would violate the gauge invariance of the electroweak La-
351 grangian, however it is experimentally known that the mediators of weak interactions are heavy
352 particles with masses $M_W = 80$ GeV and $M_Z = 91$ GeV. A possible solution of this discrepancy
353 is the mechanism of Spontaneous Symmetry Breaking.

354 The mechanism of Spontaneous Symmetry Breaking and the appearance of the mass terms
355 for W and Z bosons is realized by introducing an additional doublet of scalar fields. After that,
356 the Lagrangian is transformed in such a way that W and Z bosons acquire masses through their
357 interactions with a new particle: the Higgs boson (H). A photon does not couple to the Higgs
358 boson remaining a massless particle and leaving QED symmetry group $U(1)$ to be unbroken.

359 The measurement in this dissertation provides a test for the electroweak sector of the SM.
360 We will retrace the steps of the derivation of the electroweak part of the SM Lagrangian starting
361 from the terms for free fermions. The resulting Lagrangian accommodates electroweak gauge
362 bosons and their self-couplings. One of these self-couplings, $WW\gamma$, is the primary focus of our
363 measurement.

364 It is experimentally known that the dynamics of weak interactions depend on particle chirality
365 ([1], chapter 4.4.1). In particular, a W boson couples to left-handed fermions and right-handed
366 antifermions only. Given different properties of left-handed and right-handed fermions, they
367 are treated differently by the electroweak theory. $SU(2)$ doublets are introduced for the wave
368 functions of left-handed fermions while $SU(2)$ singlets are introduced for the wave functions of
369 right-handed fermions. Equations 3 and 4 show wave functions for the first generation fermions.
370 Wave functions for the other two generations are constructed the same way.

$$\psi_1(x) = \begin{pmatrix} u \\ d' \end{pmatrix}_L, \psi_2(x) = u_R, \psi_3(x) = d'_R. \quad (3)$$

$$\psi_1(x) = \begin{pmatrix} \nu_e \\ e^- \end{pmatrix}_L, \psi_2(x) = \nu_{eR}, \psi_3(x) = e^-_R. \quad (4)$$

The state d' in Eq. 3 is a weak eigenstate which is a linear combination of the mass eigenstates of the d , c and b quark wave functions and is determined by the quark mixing matrix, V , which is also called Cabibbo-Kobayashi-Maskawa matrix [7]:

382

$$\begin{pmatrix} d' \\ c' \\ b' \end{pmatrix} = V \begin{pmatrix} d \\ c \\ b \end{pmatrix} \quad (5)$$

To derive the unified electroweak Lagrangian, we start with the free fermion terms:

384

$$L_0 = \sum_{j=1}^3 i\bar{\psi}_j(x)\gamma^\mu\partial_\mu\psi_j(x), \quad (6)$$

where γ^μ are Dirac matrices ([1], chapter 7.1) and $\psi_j(x)$ are wave functions determined by Eqs. 3 and 4.

387

The wave function ψ_1 changes under the $SU(2)_L \times U(1)_Y$ transformations in the following way:

390

$$\psi_1(x) \rightarrow e^{iy_1\beta}U_L\psi_1(x), \quad (7)$$

while the wave functions $\psi_{(2,3)}(x)$ are singlets of $SU(2)_L$ and are affected only by $U(1)$ transformations:

393

$$\psi_{(2,3)}(x) \rightarrow e^{iy_{(2,3)}\beta}\psi_{(2,3)}(x). \quad (8)$$

The transformation in the weak isospin space is defined as $U_L \equiv e^{i\sigma_i\alpha_i/2}$ where σ_i are Pauli matrices ([1], chapter 4.2.2). Phases $\alpha_i(x)$ and $\beta(x)$ in Eqs. 7 and 8 are arbitrary functions of x , and $y_{(1,2,3)}$ are weak hypercharges which are named analogous to electric charges in QED.

397

In order for the Lagrangian to satisfy the local $SU(2)_L \times U(1)_Y$ invariance, partial derivatives in Eq. 6 have to be substituted with covariant derivatives:

400

$$D_\mu\psi_1(x) = [\partial_\mu - ig\tilde{W}_\mu(x) - ig'y_1B_\mu(x)]\psi_1(x) \quad (9)$$

$$D_\mu\psi_{(2,3)}(x) = [\partial_\mu - ig'y_{(2,3)}B_\mu(x)]\psi_{(2,3)}(x) \quad (10)$$

where g , g' are arbitrary constants,

402

$$\tilde{W}_\mu(x) \equiv \frac{\sigma_i}{2}W_\mu^i(x) = \frac{1}{\sqrt{2}} \begin{pmatrix} \sqrt{2}W_\mu^3 & (W_\mu^1 - iW_\mu^2)/\sqrt{2} \\ ((W_\mu^1 + iW_\mu^2)/\sqrt{2} & -W_\mu^3 \end{pmatrix}, \quad (11)$$

B_μ , W_μ^1 , W_μ^2 , W_μ^3 are four vector bosons that arise from the requirement that the Lagrangian is invariant under local $SU(2)_L \times U(1)$ transformations.

405

406 The Lagrangian becomes:

407

$$L_0 \rightarrow L = \sum_{j=1}^3 i\bar{\psi}_j(x)\gamma^\mu D_\mu \psi_j(x) \quad (12)$$

408 To make new vector bosons physical fields it is necessary to add terms for their kinetic energies:

409

$$L_{KIN} = -\frac{1}{4}B_{\mu\nu}B^{\mu\nu} - \frac{1}{4}W_{\mu\nu}^i W_i^{\mu\nu} \quad (13)$$

410 where $B_{\mu\nu} \equiv \partial_\mu B_\nu - \partial_\nu B_\mu$, $W_{\mu\nu}^i \equiv \partial_\mu W_\nu^i - \partial_\nu W_\mu^i + g\epsilon^{ijk}W_\mu^j W_\nu^k$

411

412 Off-diagonal terms of \tilde{W}_μ are wave functions of charged vector bosons

$$W^\pm = (W_\mu^1 \mp iW_\mu^2)/\sqrt{2} \quad (14)$$

413 while W_μ^3 and B_μ are neutral fields which are mixtures of a Z boson and a photon determined by:

414

$$\begin{pmatrix} W_\mu^3 \\ B_\mu \end{pmatrix} \equiv \begin{pmatrix} \cos\theta_W & \sin\theta_W \\ -\sin\theta_W & \cos\theta_W \end{pmatrix} \begin{pmatrix} Z_\mu \\ A_\mu \end{pmatrix} \quad (15)$$

415 where θ_W is the electroweak mixing angle and A_μ is a photon field.

416

417 In order to be consistent with QED, terms involving A_μ in the electroweak Lagrangian must
418 be equal to the corresponding terms in the QED Lagrangian [7]:

419

$$L_{QED} = i\bar{\psi}(x)\gamma^\mu \partial_\mu \psi(x) - m\bar{\psi}(x)\psi(x) + qA_\mu(x)\bar{\psi}(x)\gamma^\mu \psi(x) - \frac{1}{4}F_{\mu\nu}(x)F^{\mu\nu}(x), \quad (16)$$

420 where q is electric charge of $\psi(x)$ field, $F_{\mu\nu} \equiv \partial_\mu A_\nu - \partial_\nu A_\mu$.

421

422 This requirement relates g , g' , θ_W and e as $g \sin\theta_W = g' \cos\theta_W = e$ and provides an expres-
423 sion for weak hypercharges: $y = q - t_3$, where q is the electric charge and t_3 is the z -component of
424 the weak isospin. This results in $y_1 = 1/6$, $y_2 = 2/3$, and $y_3 = -1/3$ for quarks and $y_1 = -1/2$,
425 $y_2 = 0$, and $y_3 = -1$ for leptons. A right-handed neutrino has a weak hypercharge of $y_2 = 0$.
426 It also does not have an electric charge, and as a right-handed fermion has $t_3 = 0$, therefore, it
427 does not couple to a W boson. Thus, a right-handed neutrino does not participate in any SM
428 interaction.

429

430 Writing \tilde{W}_μ in Eq. 13 explicitly, we obtain triple gauge coupling (TGC) and quartic gauge
431 coupling (QGC) terms:

432

$$L_{TGC} = -\frac{g}{4}(\partial_\mu W_\nu^i - \partial_\nu W_\mu^i)\epsilon^{ijk}W^{\mu j}W^{\nu k} - \frac{g}{4}\epsilon^{ijk}W_\mu^j W_\nu^k(\partial^\mu W^{\nu i} - \partial^\nu W^{\mu i}) \quad (17)$$

$$L_{QGC} = -\frac{g^2}{4}\epsilon^{ijk}\epsilon^{ilm}W_\mu^j W_\nu^k W^{\mu l}W^{\nu m} \quad (18)$$

433 Substituting expressions for W_μ^i and B_μ determined by Eqs. 14 and 15 into Eqs. 17 and 18 we
434 receive charged TGC and QGC terms in the Lagrangian (those involving two or four W bosons)
435 in the forms of Eqs. 19 and 22, but all neutral TGC and QGC terms (those not involving any
436 W bosons) cancel out.

437 Equation 19 involves WWZ (Eq. 20) and $WW\gamma$ (Eq. 21) interactions:

438

$$L_{TGC} = L_{TGC}^{(1)} + L_{TGC}^{(2)}, \quad (19)$$

$$L_{TGC}^{(1)} = -ie \cot \theta_W (W^{-\mu\nu} W_\mu^+ Z_\nu - W^{+\mu\nu} W_\mu^- Z_\nu + W_\mu^- W_\nu^+ Z^{\mu\nu}), \quad (20)$$

$$L_{TGC}^{(2)} = -ie (W^{-\mu\nu} W_\mu^+ A_\nu - W^{+\mu\nu} W_\mu^- A_\nu + W_\mu^- W_\nu^+ A^{\mu\nu}). \quad (21)$$

439 Equation 22 involves $WWWW$ (Eq. 23), $WWZZ$ (Eq. 24), $WWZ\gamma$ (Eq. 25), and $WW\gamma\gamma$
 440 (Eq. 26) interactions:

441

$$L_{QGC} = L_{QGC}^{(1)} + L_{QGC}^{(2)} + L_{QGC}^{(3)} + L_{QGC}^{(4)}, \quad (22)$$

$$L_{QGC}^{(1)} = -\frac{e^2}{2 \sin^2 \theta_W} (W_\mu^+ W^{-\mu} W_\nu^+ W^{-\nu} - W_\mu^+ W^{\mu+} W_\nu^- W^{-\nu}), \quad (23)$$

$$L_{QGC}^{(2)} = -e^2 \cot^2 \theta_W (W_\mu^+ W^{-\mu} Z_\nu Z^\nu - W_\mu^+ Z^\mu W_\nu^- Z^\nu), \quad (24)$$

$$L_{QGC}^{(3)} = -e^2 \cot \theta_W (2W_\mu^+ W^{-\mu} Z_\nu A^\nu - W_\mu^+ Z^\mu W_\nu^- A^\nu - W_\mu^+ A^\mu W_\nu^- Z^\nu), \quad (25)$$

$$L_{QGC}^{(4)} = -e^2 (W_\mu^+ W^{-\mu} A_\nu A^\nu - W_\mu^+ A^\mu W_\nu^- A^\nu). \quad (26)$$

442 In the measurement of this dissertation we probe $WW\gamma$ coupling (Eq. 21).

443

444 The unified electroweak Lagrangian discussed above involves kinetic energy terms for fermions
 445 and gauge bosons as well as interactions of fermions with gauge bosons, TGC, and QGC. How-
 446 ever, this Lagrangian does not contain any mass terms. Because left-handed and right-handed
 447 wave functions transform differently under the electroweak symmetry, adding fermion mass terms
 448 of $\frac{1}{2}m_f^2 \bar{\psi}\psi$ would violate the Lagrangian invariance and, therefore, fermion mass terms are for-
 449 bidden by the $SU(2) \times U(1)$ symmetry requirement. Mass terms for gauge bosons also would
 450 violate the Lagrangian invariance just as a photon mass term $\frac{1}{2}m^2 A^\mu A_\mu$ would violate $U(1)$
 451 invariance of L_{QED} [1]. Therefore, Lagrangian L in Eq. 12 contains massless particles only.

452

453 However, it is known from experiments that the Z and W bosons as well as fermions are mas-
 454 sive particles and, therefore, our theory should accommodate their masses. To introduce masses
 455 into the electroweak Lagrangian, an $SU(2)_L$ doublet of complex scalar fields $\phi(x)$ is added to
 456 the Lagrangian:

457

$$\phi(x) \equiv \begin{pmatrix} \phi^{(+)}(x) \\ \phi^{(0)}(x) \end{pmatrix} \quad (27)$$

458 By selecting a special gauge of $\phi(x)$ it is possible to spontaneously break electroweak sym-
 459 metry, generate a new scalar particle, the Higgs boson [7], and introduce mass terms for W and
 460 Z bosons and charged fermions through their couplings to the Higgs boson. The strength of the
 461 coupling constant is proportional to the square of the particle's mass, therefore, heavier particles
 462 are more likely to interact with H , and massless particles do not couple to H .

463

464 The mechanism of generating a fermion's mass involves both left-handed and right-handed
 465 components of the fermion. If our hypothesis that right-handed neutrinos do not exist is right,
 466 then the Higgs mechanism does not generate neutrino masses. However, from the experiments
 467 of neutrino oscillations, neutrinos are known to have masses even though they are orders of
 468 magnitude smaller than those of other fermions. Several hypotheses have been offered to resolve
 469 this contradiction however at the moment the mechanism for neutrinos to acquire masses remain
 470 unknown [5].

471

472 In this dissertation, we study an electroweak process $W\gamma \rightarrow l\nu_l\gamma$ and probe the TGC vertex
 473 $WW\gamma$ (Eq. 21). To do that, we measure the differential cross section of $W\gamma \rightarrow l\nu_l\gamma$ with respect

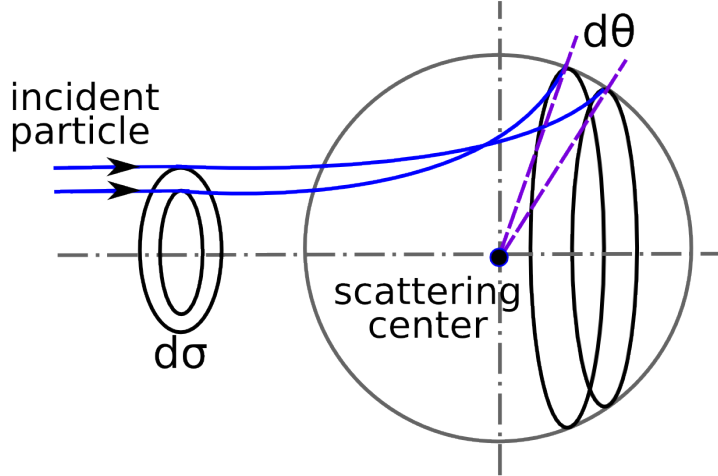
⁴⁷⁴ to the photon transverse momentum. The concept of the cross section in particle physics is
⁴⁷⁵ discussed in the next chapter.

⁴⁷⁶

477 2.2 Cross Section and Luminosity

478 In this dissertation we measure the total cross section of the process $pp \rightarrow l\nu\gamma + X$ and its dif-
 479 ferential cross section in transverse momentum of the photon. A cross section in particle physics
 480 is an interaction probability per unit flux of incident particles [12]. It can be interpreted as an
 481 area which must be crossed by an incident particle in order to interact with a scattering center,
 482 or, in case of a differential cross section, area $d\sigma$ within which an incident particle must appear
 483 to be scattered off by an angle $d\theta$ (Fig. 8). The relationship between $d\sigma$ and $d\theta$ gives us the
 484 expression for a differential cross section $d\sigma/d\theta$. Integrating over $d\theta$, we obtain the total cross
 485 section σ . The cross section concept illustrated in Fig. 8 is generalized to be an effective area,
 486 and is generalized for two (or more) particle interactions rather than a light particle scattering
 487 off a stationary center.

488 The angle θ here is used only as an illustration of a concept of differential cross section. In
 489 particle physics we measure a differential cross section with respect to a parameter X which can
 490 be a parameter of one of final state particles or of a system of final state particles. For example,
 491 a cross section could be measured as a function of the transverse momentum of a final state
 492 photon P_T^γ , the invariant mass of two final state leptons m_{ll} , or even discreet observables such
 493 as the number of jets associated with the process N_{jets} .



495 Figure 8: Illustration of the differential cross section concept in the classical case.

496 In the scenario illustrated in Fig. 8, the number of particles passing through the area σ per
 497 unit time is $N = L \cdot \sigma$, where L is the flux of incident particles and is called luminosity. For
 498 colliding beams, the luminosity is determined by collisions frequency, the number of colliding
 499 particles in each beam, and beams cross sections. The cross section σ of a specific process can
 500 be determined from an experiment as $\sigma = N/L$.

501

502 A cross section can be computed theoretically using the following expression:

503

$$\sigma = \frac{W_{fi}}{F} N_{fs}, \quad (28)$$

504 where W_{fi} is a transition probability between final and initial states of the system per unit spatial
 505 volume, F is the initial flux, and N_{fs} is the density of final states ([8], chapter 4.3). The initial
 506 flux in this expression is determined as number of incident particles per unit volume multiplied

507 by their velocity and by the number of target particles per unit volume.

508

509 The formula for the cross section relevant for our measurement, two particles to three final
510 state particles scattering $1 + 2 \rightarrow 3 + 4 + 5$, is determined by the Fermi's Golden Rule [1]:

511

$$\sigma = \frac{1}{4\sqrt{(p_1 p_2)^2 - (m_1 m_2)^2}} \int |M|^2 (2\pi)^4 \delta^4(p_1 + p_2 - p_3 - p_4 - p_5) \prod_{j=3}^5 \frac{1}{2\sqrt{\bar{p}_j^2 + m_j^2}} \frac{d^3 \bar{p}_j}{(2\pi)^3}, \quad (29)$$

512 where p_i are four-momenta and \bar{p}_i are three momenta of the initial state and the final state
513 particles, m_i are masses of particles, M is the process amplitude determined by the dynamics
514 of the particles interaction. All possible momenta of the final state particles is called the phase
515 space.

516

517 During proton-proton collisions at high energy, the hard scattering process occurs between
518 partons in the protons, as discussed in Ch. 1.4. Therefore, the cross section of a process
519 $pp \rightarrow X + Y$ has two ingredients: PDFs and a partonic cross section $\sigma_{ab \rightarrow X}$. The partonic
520 cross section is described by perturbative QCD while PDFs require non-perturbative computa-
521 tions and are determined, in part, from experiments (Fig. 7). According to the QCD factorization
522 theorem [9]:

523

$$\sigma(pp \rightarrow X + Y) = \sum_{a,b} \int dx_a dx_b f_a(x_a, Q^2) f_b(x_b, Q^2) \sigma(ab \rightarrow X). \quad (30)$$

524 In the case of $W\gamma$ process, X is $l\nu\gamma$, ab are $q_i \bar{q}_j$ or $q_j \bar{q}_i$. Q^2 is the large momentum scale
525 that characterizes hard scattering, f_a and f_b are PDFs, x_a and x_b are fractions of momenta of
526 the partons. In the next sections we will discuss the computation of partonic cross sections of
527 the $W\gamma$ process and possible BSM effects.

528

2.3 Standard Model $W\gamma$ Production

A W boson in proton-proton collisions can be produced in the processes $q\bar{q}' \rightarrow W$ where q and \bar{q}' are a quark and an antiquark which have a total charge of +1 if producing a W^+ boson or -1 if producing a W^- boson. The processes $u\bar{d} \rightarrow W^+$ and $d\bar{u} \rightarrow W^-$ are the most likely to occur because u and d are valence quarks in a proton. There are twice as many u quarks in a proton as d quarks, therefore, W^+ is produced twice more frequently than W^- . Antiquarks \bar{d} and \bar{u} come from the sea $q\bar{q}$ pairs of the other proton.

Once created, a W boson decays immediately, its lifetime is $\simeq 10^{-25}$ s. In an experiment one detects its decay products rather than the W boson itself. Decay modes of a W boson include $W^\pm \rightarrow l^\pm \nu_l (\bar{\nu}_l)$ where $l^\pm = e^\pm, \mu^\pm$ or τ^\pm with branching fractions of 11% per a leptonic channel [5]. The remaining 67% account for various $W \rightarrow q\bar{q}'$ decays. In this dissertation we only consider $W^\pm \rightarrow \mu^\pm \nu_\mu (\bar{\nu}_\mu)$ and $W^\pm \rightarrow e^\pm \nu_e (\bar{\nu}_e)$ channels.

A photon can be emitted from any charged particle of the process: a quark, an antiquark, a charged lepton or a W boson (Fig. 9, top). A quark and an antiquark are initial state particles and, therefore, if one of them radiates a photon, we refer to the process as initial state radiation (ISR). A muon or an electron is a final state particle and if it radiates a photon, we call such a process final state radiation (FSR). Finally, a W boson is a gauge boson and if it radiates a photon, the process has a vertex with three gauge bosons: $WW\gamma$, and we call such process the triple gauge coupling (TGC). We cannot distinguish between these processes experimentally because we detect final state particles only.

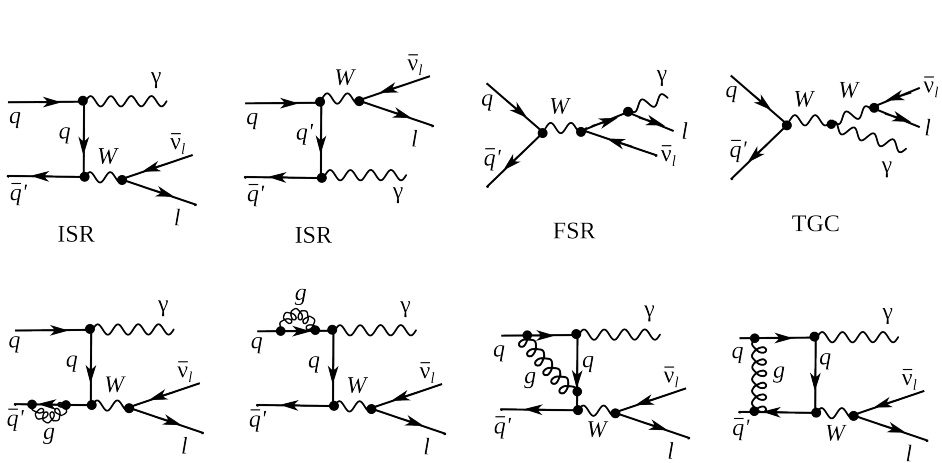


Figure 9: Feynman diagrams of $W\gamma$ production. Top: LO diagrams, bottom: several examples of NLO in QCD.

The electroweak Lagrangian is described in Chapter 2.1. It is possible to derive equations of motion from the Lagrangian for any fields involved [1]. However, in a quantum field theory equations of motion cannot be solved exactly and, therefore, the perturbative approach is used if a coupling constants is $g \ll 1$.

To represent the process graphically Feynman diagrams were invented. Also the diagrams can be used to calculate the process amplitude M in Eq. 29 because they are determined by Lagrangian terms relevant to the process. There are an infinite number of Feynman diagrams corresponding to any specific process and the total amplitude of the process is a sum of individual amplitudes of each diagram and it is not technically possible to take into account all of them. Each vertex introduces a factor in the amplitude of the process that is proportional to

563 the coupling constant. If the coupling constant is $g \ll 1$, the perturbative approach arranges
564 all the diagrams by orders of contribution, and, therefore, the Feynman diagrams with fewer
565 vertices would give a significantly larger contribution to the amplitude. In Fig. 9 examples of
566 the Leading Order (LO) and the Next-to-Leading Order (NLO) Feynman diagrams are shown
567 (top and bottom diagrams respectively).

568

569 At LO, the $W\gamma$ process is represented by four Feynman diagrams including one FSR, one
570 TGC and two ISR diagrams. Each LO diagram has three vertices. The first calculation of the
571 $W\gamma$ process with necessary expressions can be found in [14].

572

573 The NLO corrections to the amplitude of the $W\gamma$ process that are shown in Fig. 9 are QCD
574 corrections only, which include gluon loops at the same quark line and exchange of a gluon be-
575 tween two different quark lines, however, QED and weak NLO diagrams are also possible. QED
576 corrections involve radiations of extra photons by charged particles, exchange of photons be-
577 tween different charged particles or a photon can be radiated and absorbed by the same charged
578 particle forming a loop. Similarly, weak corrections involve extra virtual W or Z bosons. The
579 QCD corrections are the largest among the discussed correction types because the QCD coupling
580 constant is the largest.

581

582 A theoretical cross section in particle physics is compared to a measurement result to test the predictions of the model. Also the theoretical cross section is used for producing simulated data. In a simulation, a large set of pp collisions resulting in a physics process of interest is modeled to create a data set that mimics real data. A typical simulation consists of two parts: the generation of the process and the simulation of particles paths through the detector. The first stage contains a collection of events with final state particles with kinematic quantities distributed according to theoretical predictions for a given process. This stage relies on the theory including the cross section and also all dynamics of the process. The second stage simulates the interaction with media during propagation of particles through the model of the detector as well as the response of detector electronics. In its final form, a simulated dataset has the same format and content of detector signals for each event as real data, and can undergo the same reconstruction and analysis procedure as real data would.

594

595 The most precise theoretical $W\gamma$ cross section available is the Next-to-Next-to-Leading Order
596 (NNLO) cross section in QCD [15]. The effects of the NNLO correction over the NLO correction
597 and over the LO result are shown in Fig. 10 for the transverse mass of the final state particles
598 $m_T^{l\nu\gamma}$ and for the rapidity difference between a charged lepton and a photon $\Delta_{l\gamma}$. The NNLO and
599 NLO theoretical predictions for the photon transverse momentum p_T^γ are overlaid with the 7 TeV
600 ATLAS result. The contribution from higher order corrections is estimated to be $\pm 4\%$. However,
601 the NNLO theoretical result was published only recently, in 2015, and no NNLO $W\gamma$ simulation
602 is available at this time. The simulation used in this analysis is LO + up to two hadronic jets
603 simulation which was found to give the same predictions as the NLO result.

604

605 Certain BSM theories predict an enhancement of the contribution from the TGC diagram
606 over the SM prediction. The discussion of these BSM effects and how they affect the $W\gamma$ process
607 takes place in Ch. 2.4.

608

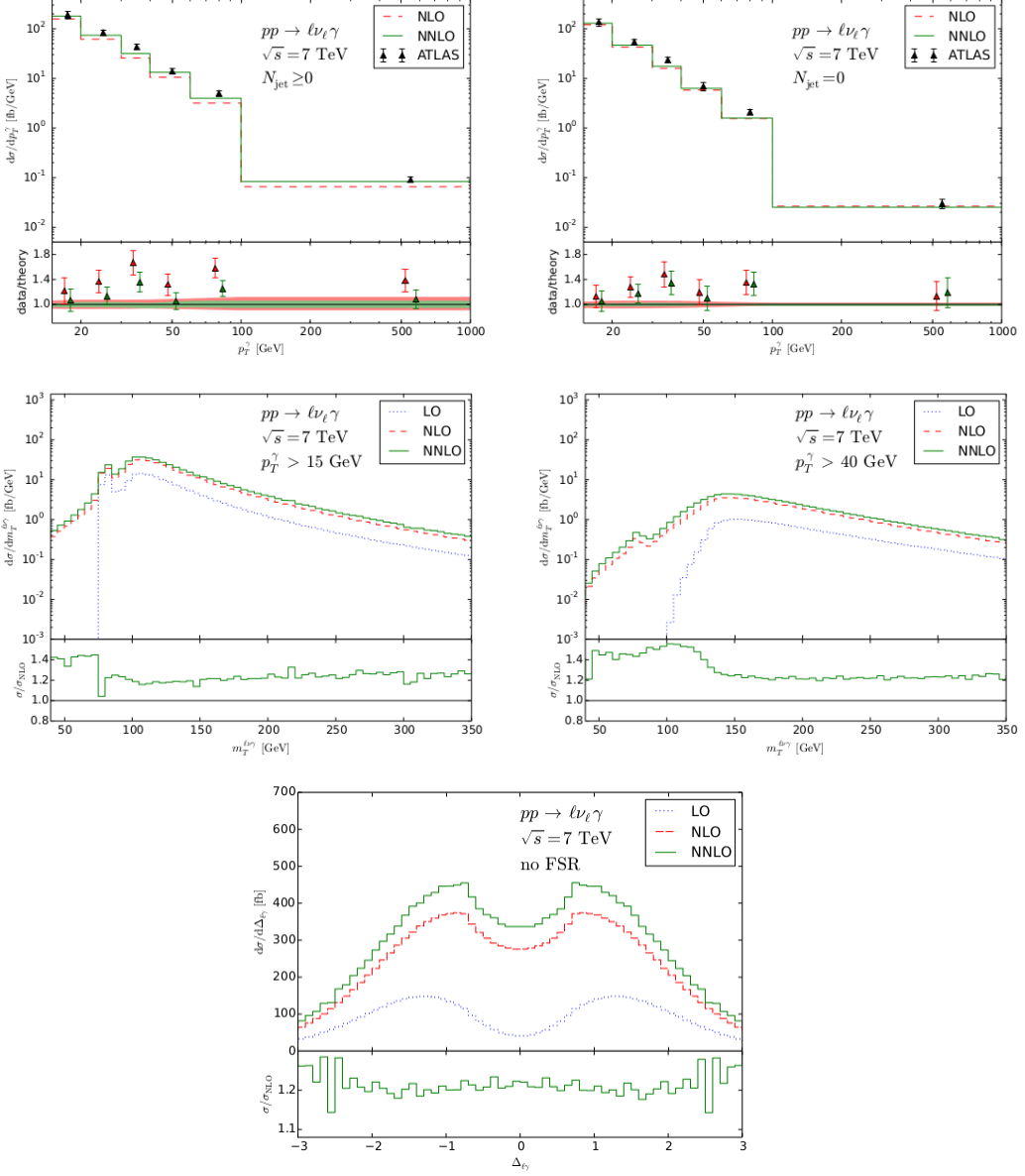


Figure 10: Theory spectra. Top: NLO and NNLO p_T^γ spectra of $W\gamma \rightarrow l\nu\gamma$ at $\sqrt{s} = 7$ TeV overlaid with ATLAS data for $N_{jet} \geq 0$ (left) and $N_{jet} = 0$ (right). Middle: LO, NLO and NNLO $m_T^{l\nu\gamma}$ spectra of $W\gamma \rightarrow l\nu\gamma$ at $\sqrt{s} = 7$ TeV for $P_T^\gamma > 15$ GeV (left) and $P_T^\gamma > 40$ GeV (right). Bottom: LO, NLO and NNLO $\Delta_{l\gamma}$ spectra of $W\gamma \rightarrow l\nu\gamma$ at $\sqrt{s} = 7$ TeV.

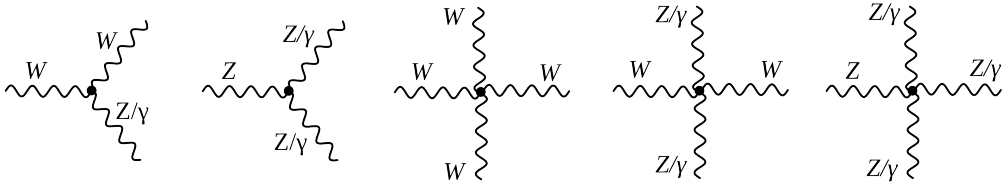
609 2.4 Anomalous $W\gamma$ Production

610 Most BSM physics theories predict the existence of particles with masses lying beyond the dis-
 611 covered energy range. If their masses are not accessible even at the accelerators with the highest
 612 energies, the direct detection of such particles is not possible. However, loops of heavy particles
 613 can affect diagrams of productions of lighter particles. They would give additional contributions
 614 to TGC and QGC couplings and, therefore, to the amplitudes to the processes involving TGC
 615 and QGC productions. There would be a different number of events produced in the process
 616 than one would expect based on SM predictions as shown in Fig. 12.

617

618 TGC and QGC couplings can be probed by precision measurements of SM processes of diboson
 619 and triboson productions because these processes can occur through TGC and QGC. TGC
 620 and QGC are represented by vertices with three and four bosons (Fig. 11). As discussed in
 621 Ch. 2.1, charged TGC and QGC are possible at tree level in the SM while neutral TGC and
 622 QGC are not.

623



624 Figure 11: Charged TGC (first), neutral TGC (second), charged QGC (third and fourth), and
 625 neutral QGC (fifth) vertices.

626 To account for the effects from the potential loops of heavy particles, we introduce an ef-
 627 fective Lagrangian with arbitrary values of coupling constants which can be reduced to the SM
 628 Lagrangian if these constants would have their SM values. Introducing the effective Lagrangian
 makes searches model-independent because we do not specify particles that form the loops but
 instead just check whether there is a deviation from the SM prediction in measured observables.

629

630 In $W\gamma$ measurement we can probe $WW\gamma$ vertex. The most general Lorentz invariant La-
 631 grangian terms of $WW\gamma$ interaction takes the following form [17]:

632

$$633 iL_{eff}^{WW\gamma} = iL_{eff(1)}^{WW\gamma} + iL_{eff(2)}^{WW\gamma} + iL_{eff(3)}^{WW\gamma}, \quad (31)$$

634 where

$$iL_{eff(1)}^{WW\gamma} = e[g_1^\gamma A^\mu (W_{\mu\nu}^- W^{+\nu} - W_{\mu\nu}^+ W^{-\nu}) + \kappa_\gamma W_\mu^+ W_\nu^- A^{\mu\nu} + \frac{\lambda_\gamma}{m_W^2} A^{\mu\nu} W_\nu^{+\rho} W_{\rho\mu}^-], \quad (32)$$

$$iL_{eff(2)}^{WW\gamma} = e[i g_5^\gamma \epsilon_{\mu\nu\rho\sigma} ((\partial^\rho W^{-\mu}) W^{+\nu} - W^{-\mu} (\partial^\rho W^{+\nu})) A^\sigma + i g_4^\gamma W_\mu^- W_\nu^+ (\partial^\mu A^\nu + \partial^\nu A^\mu)], \quad (33)$$

$$iL_{eff(3)}^{WW\gamma} = e[\frac{\tilde{\kappa}_\gamma}{2} W_\mu^- W_\nu^+ \epsilon^{\mu\nu\rho\sigma} A_{\rho\sigma} - \frac{\tilde{\lambda}_\gamma}{2m_W^2} W_{\rho\mu}^- W_\nu^{+\mu} \epsilon^{\nu\rho\alpha\beta} A_{\alpha\beta}], \quad (34)$$

635 where e is the absolute value of the electron charge, A^μ is the photon field, $W^{\pm\mu}$ are the fields
 636 of the W^\pm bosons, $W_{\mu\nu} = \partial_\mu W_\nu - \partial_\nu W_\mu$, $A_{\mu\nu} = \partial_\mu A_\nu - \partial_\nu A_\mu$, m_W is the mass of the W boson,

637 g_1^γ , κ_γ , λ_γ , g_5^γ , g_4^γ , $\tilde{\kappa}_\gamma$, and $\tilde{\lambda}_\gamma$ are constants.

638

639 Despite seven constants in the extended Lagrangian, only λ_γ and κ_γ are considered in the
 640 aTGC searches. The rest of the constants are fixed to their SM values based on the following
 641 considerations. The constants $g_1^\gamma = 1$ and $g_5^\gamma = 0$ are fixed to make the Lagrangian obey the
 642 electromagnetic gauge invariance for the on-shell photons. The non-zero value of g_5^γ also violates
 643 C and P conservations, and non-zero values of g_4^γ , $\tilde{\kappa}_\gamma$, $\tilde{\lambda}_\gamma$ violate the CP conservation law. Such
 644 violation parametrizations are not considered in charged TGC measurements, thus, constants
 645 g_4^γ , $\tilde{\kappa}_\gamma$, and $\tilde{\lambda}_\gamma$ are fixed to zero.

646

647 The SM values of λ_γ and κ_γ are $\lambda_\gamma = 0$ and $\kappa_\gamma = 1$. For convenience, the deviation from the
 648 SM value is introduced $\Delta\kappa_\gamma \equiv \kappa_\gamma - 1$. These two parameters are tested in $WW\gamma$ aTGC searches
 649 because non-zero values of these parameters would not violate any fundamental law.

650

651 The most significant effects of aTGC would appear at high energy scales. Figure 12 shows
 652 this effect in P_T^γ spectrum of 7 TeV $W\gamma \rightarrow \mu\nu\gamma$ measurement. As seen in Fig. 12, the spectrum
 653 with non-zero values of aTGC constants at low P_T^γ coincides with the SM prediction but for
 654 higher P_T^γ the disagreement appears.

655

656 A common approach to aTGC searches is to measure the spectrum of a kinematic parameter
 657 highly correlated with the energy of a final state particle or a system of final state particles. For
 658 $W\gamma$ process, the most sensitive variable is P_T^γ . Examining this spectrum allows us to probe and
 659 constrain aTGC coupling constants. Chapter 2.5 reviews the experimental results to date on
 660 constraining aTGC coupling constants of the $WW\gamma$ vertex.

661

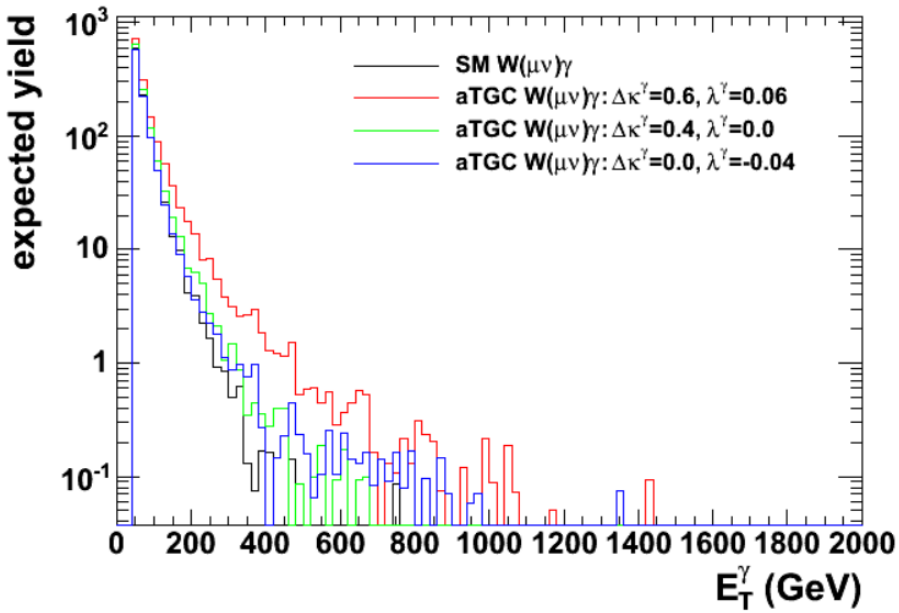


Figure 12: Distributions of P_T^γ in simulated $W\gamma \rightarrow \mu\nu\gamma$ events with different values of aTGC constants at LHC energy of $\sqrt{s} = 7$ TeV. Source of figure: [18].

662 2.5 A brief history of $W\gamma$ measurements

663 aTGC parameters of the $WW\gamma$ vertex can be probed in measurements of $W\gamma$, WW , WZ
 664 processes. Limits on the $\Delta\kappa_\gamma$ and λ_γ constants obtained by different experiments are summa-
 665 rized in Fig. 13. The summary includes the combination results from D0 [19] and LEP [20]
 666 as well as results of several individual measurements by ATLAS and CMS including $W\gamma$ at
 667 $\sqrt{s} = 7$ TeV [21], [22], WW at $\sqrt{s} = 7$ and 8 TeV [23], [24], [25], and WV at $\sqrt{s} = 7$ and 8 TeV [26], [28]
 668 measurements.

669

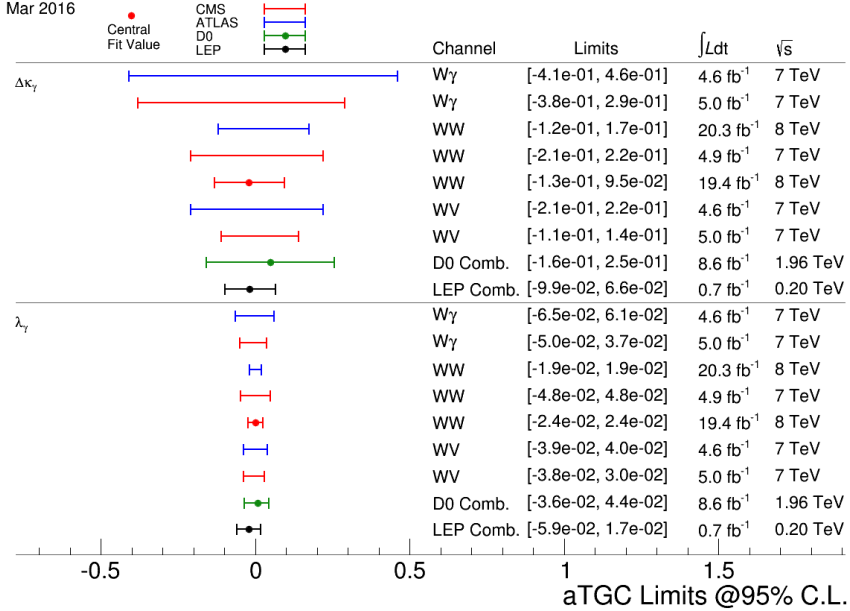


Figure 13: Summary of limits on the $WW\gamma$ aTGC coupling constants. Figure from [27].

670 The most recent measurements of $W\gamma$ production were performed by CMS [22] and AT-
 671 LAS [21] collaborations with pp collisions at $\sqrt{s} = 7$ GeV collected in 2011. Both collaborations
 672 considered two channels: $W\gamma \rightarrow \mu\nu\gamma$ and $W\gamma \rightarrow e\nu\gamma$.

673

674 Diboson processes are rare in pp -collisions and analysts have to filter out events of their in-
 675 terest from many processes which are more likely to happen. To do that, a variety of selection
 676 criteria are applied which reject most of the background events to increase the signal fraction
 677 in the selected sample as much as possible. However, even after all possible selection criteria
 678 are applied, the majority of selected events are still background events and it is not possible to
 679 reduce the background any further without also significantly reducing signal.

680

681 The major source of such irreducible background is the fake photon background where
 682 hadronic jets are misidentified as photons. Such events originate mostly from $W+jets$, but
 683 $Z+jets$ and $t\bar{t}+jets$ events contribute to this source of background as well. In the electron chan-
 684 nel there is one more significant background that is the fake photon background where electron
 685 is misidentified as a photon. Such events are coming from $Z+jets$ events. For the muon channels
 686 this background is small. Other sources of backgrounds for both channels include real- γ , fake
 687 lepton + real photon and fake lepton + fake photon backgrounds. The major source of real- γ
 688 background is the $Z\gamma$ process where a final state lepton and a photon mimics the $W\gamma$ final
 689 state. Fake lepton + real photon background originates from the $\gamma+jets$ process where a jet is
 690 misidentified as a lepton. Fake lepton + fake photon backgrounds come from dijet and multijet
 691 events where one of the jets is misidentified as a lepton and the other one is misidentified as
 692 a photon. The probability of a jet to be misidentified as a lepton is very small, therefore fake

lepton + real photon and fake lepton + fake photon backgrounds are negligible.

P_T^γ spectra are measured because this variable is the most sensitive to the potential aTGC. The P_T^γ spectra of the selected events in data superimposed with selected events in the simulation of the signal and estimated background contribution for the muon and electron channels are shown in Fig. 14 for CMS and in Fig. 15 for ATLAS measurement. Both measurements show a good agreement between data and the simulation.

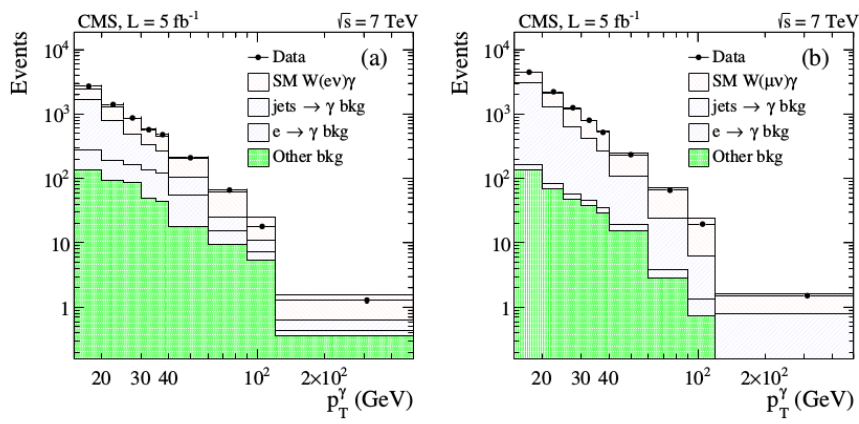


Figure 14: The distribution of the p_T^γ of $W\gamma$ candidates in the analysis of 7 TeV CMS data. Data vs signal MC + background estimates. Left: $W\gamma \rightarrow e\nu\gamma$, right: $W\gamma \rightarrow \mu\nu\gamma$ [22].

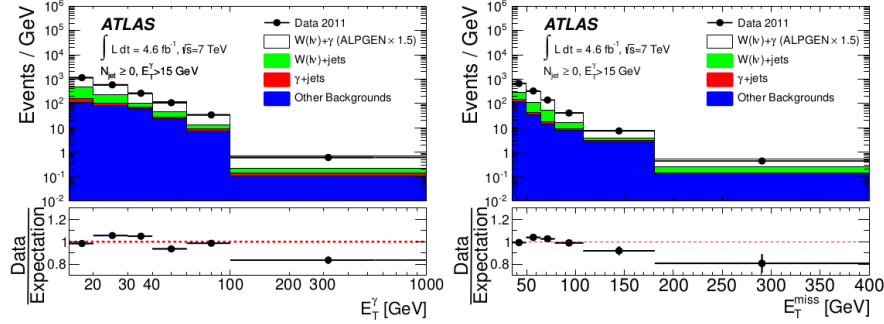


Figure 15: The distribution of the photon transverse momentum (left) and missing transverse momentum (right) of $W\gamma$ candidates in the analysis of 7 TeV ATLAS data. Data vs signal MC + background estimates [21].

The phase space restrictions of $W\gamma$ measurements come from the considerations of the detector acceptance, reducing heavily background-dominated regions and theoretical considerations such as to avoid divergence of the cross section and to reduce ISR and FSR contributions to the cross section.

CMS provides measurements of the P_T^γ spectrum, the total cross section within the phase spaces of $\Delta R > 0.7$, $P_T^\gamma > 15$ GeV, $P_T^\gamma > 60$ GeV and $P_T^\gamma > 90$ GeV.

ATLAS, in addition to the P_T^γ spectrum, total cross section and limits, provides the differential cross section and cross section with different number of associated jets. The phase space restrictions for ATLAS measurement include requirements on charged lepton kinematics $P_T^l > 25 \text{ GeV}$, $|\eta_l| < 2.47$, requirements on the transverse momentum of a neutrino $P_T^\nu > 35 \text{ GeV}$, photon kinematics $P_T^\gamma > 15 \text{ GeV}$, $|\eta^\gamma| < 2.37$, photon isolation fraction $\epsilon_h^P < 0.5$ and lepton-photon separation $\Delta R(l, \gamma) > 0.7$. For the differential cross section in number of associated jets, the requirements on jets kinematics and jets separation from leptons and photons are also applied: $E_T^{jet} > 30 \text{ GeV}$, $|\eta^{jet}| < 4.4$, $\Delta R(e/\mu/\gamma, jet) > 0.3$. No evidence of new physics is observed.

The estimated cross sections with any number of associated jets for $P_T^\gamma > 15 \text{ GeV}$ are

$$\sigma(pp \rightarrow W\gamma \rightarrow l\nu\gamma) = 37.0 \pm 0.8 \text{ (stat.)} \pm 4.0 \text{ (syst.)} \pm 0.8 \text{ (lumi.) pb} \quad (35)$$

and

$$\sigma(pp \rightarrow W\gamma \rightarrow l\nu\gamma) = 2.77 \pm 0.03 \text{ (stat.)} \pm 0.33 \text{ (syst.)} \pm 0.14 \text{ (lumi.) pb} \quad (36)$$

for CMS and ATLAS respectively. The results agree with NLO MCFM [?] predictions of $31.81 \pm 1.8 \text{ pb}$ for the phase space used by CMS and of $1.96 \pm 0.17 \text{ pb}$ for the phase space used by ATLAS.

In addition to the cross sections, both CMS and ATLAS provide limits on aTGC coupling constants $\Delta\kappa_\gamma$ and λ_γ . To do that, samples with non-zero aTGC coupling constants are generated, run through the whole reconstruction and selection procedures, and compared to the measured results of P_T^γ spectra. The results on one-dimensional limits are quoted in Fig. 13 while the results on two-dimensional limits can be found in [21], [22].

In this dissertation we are measuring total and differential $d\sigma/dP_T^\gamma$ cross section. While the aTGC limits are not derived in this dissertation, the measured differential cross section can be used to derive them. The measurement details and results are described in Chapter 5.

736 **3 Experimental Setup**

737 3.1 Large Hadron Collider

738 The Large Hadron Collider (LHC) [31], [32], [33] is the largest particle accelerator and the most
739 ambitious particle physics research facility ever built. The LHC is placed into a tunnel originally
740 built for the LEP accelerator. The LEP was decommissioned to make room for the LHC. The
741 tunnel is about 27 km in circumference, located at the Swiss-French boundary up to 100 meters
742 undergroud.

743 Before entering LHC, particle beams are going through several stages of the acceleration and
744 the LHC is the last element of the chain of the CERN's accelerator complex (Fig. 16). Protons
745 are extracted from hydrogen atoms, are accelerated by Linac2 to energies of 5 MeV, then injected
746 into the Proton Synchrotron Booster (PSB) where they reach energies of 1.4 GeV. After that
747 protons are sent to PS and Super PS (SPS) where they are accelerated up to 25 GeV and 450 GeV
748 respectively. Finally, protons enter the LHC and are accelerated to reach their collision energies
749 of several TeV per beam. Besides protons, the complex also accelerates and collides lead ions
750 however in this dissertation we analyze data from proton-proton collisions only and, therefore,
751 are not discussing lead ion collisions.

752 Main goals of LHC were to detect the SM Higgs boson if it existed and to search for evidences
753 of BSM physics which may give a clue on understanding the phenomena including but not limited
754 to the dark matter, the matter-antimatter asymmetry, the nature of the gravitational force. Six
755 detectors are installed at the LHC to detect particles and perform the relevant measurements.
756 There are general purpose detectors ATLAS and CMS, there is LHCb which specializes of the
757 physics of B-mesons, and ALICE which is designed to detect products of heavy ion collisions. In
758 addition, there are two relatively small detectros: LHCf and TOTEM which are installed close
759 to the ATLAS and CMS collision points respectively.

760 The design energy of the LHC is 7 TeV per beam however several lower energy points were
761 and are being probed. In 2010-2011 the LHC operated at energy of 3.5 TeV per beam which was
762 already higher than energy of any other collider. In 2012 the energy increased up to 4 GeV. In
763 2013-2014 the LHC was shut down for upgrades. Collisions were restarted at 6.5 TeV in 2015
764 and the LHC is still operating at this energy in 2016.

765 All important measurements performed at lower energies are also repeated at higher energies
766 because the ability to probe higher energy scales increases our chances for a discovery and even
767 if no deviations from the known physics are found at a given energy point, the discovery is still
768 possible to happen as we go higher in the energy.

769 The greatest achievement by the LHC today is the discovery of the Higgs boson in 2012 by
770 the CMS [3] and the ATLAS [4] collaborations in 2012.

771 While different BSM searches have been constituting a significant part of the LHC physics
772 program since the beginning of its operation, no deviations from the SM were found by any of
773 the experiments. The searches continue with higher beam energies and larger amount of data.

774 In addition to the beam energy, there are many other collider parameters. A brief summary
775 of them is available in Tab. 2. One of the most important parameters of an accelerator is the
776 ability to produce a large number of interesting collisions which is determined by the luminosity.
777 The instantaneous luminosity is determined by the following expression [5]:

$$778 \quad L = f \frac{n_1 n_2}{4\pi\sigma_x\sigma_y}$$

779 where n_1 and n_2 are numbers of particles in colliding bunches, f is a frequency of collisions,
780 σ_x and σ_y are beam sizes in horizontal and vertical directions. To determine the integrated
781 luminosity, one has to integrate the instantaneous luminosity over time:

792 $L_{int} = \int L dt$

793

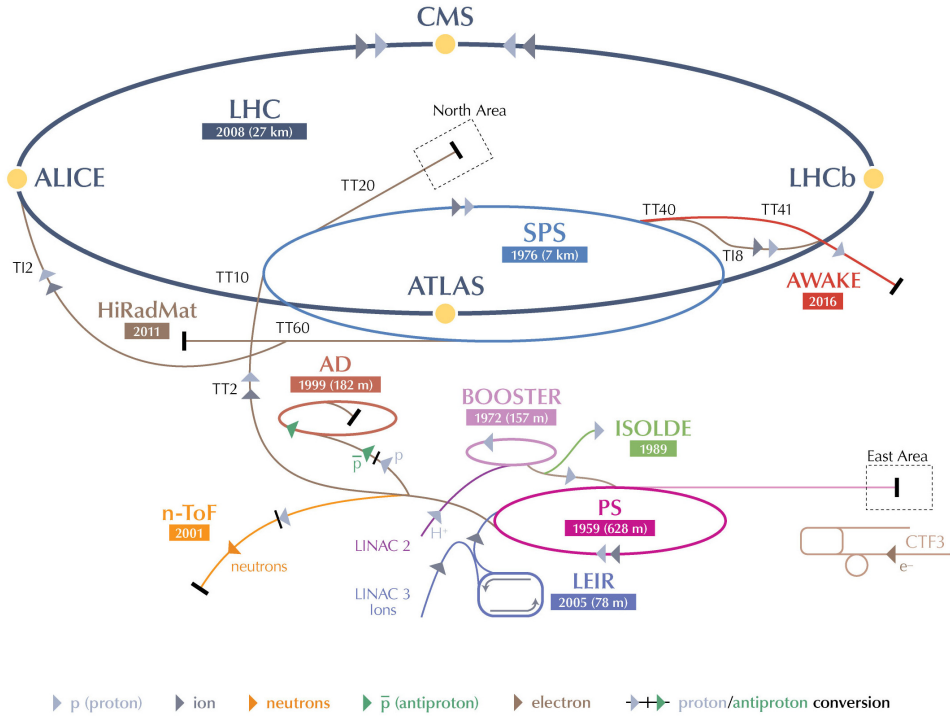
794 The luminosity of the LHC is also higher than of any previously existed collider. The integrated
 795 luminosity of the LHC for pp collisions for different years of the operation is shown in Fig. 17.
 796 Run periods of LHC in 2010-2012 refer to Run I of the LHC operation. While working on energy
 797 of $\sqrt{s} = 7$ TeV, LHC delivered 45 pb^{-1} and 6.1 fb^{-1} of data in 2010 and 2011 year respec-
 798 tively. In 2012 the working energy of LHC was $\sqrt{s} = 8$ TeV, and the integrated luminosity
 799 was $L_{int} = 23.3 \text{ fb}^{-1}$. After a long shutdown, LHC was upgraded for Run II, to operate on
 800 $\sqrt{s} = 13$ TeV in 2015 and delivered 4.2 fb^{-1} of data by the end of 2015. In 2016 LHC continued
 801 operating at $\sqrt{s} = 13$ TeV and delivered the integrated luminosity of 41.1 fb^{-1} [37].

802

803 The measurement of this dissertation is performed at the energy of 4 TeV per beam or at
 804 the center of mass energy $\sqrt{s} = 8$ TeV with 19.6 fb^{-1} of data. The same process was measured
 805 at $\sqrt{s} = 7$ TeV with about four times less amount of data by both CMS and ATLAS. These
 806 measurements are discussed in greater details in Ch. 2.5.

807

CERN's Accelerator Complex



LHC Large Hadron Collider SPS Super Proton Synchrotron PS Proton Synchrotron

AD Antiproton Decelerator CTF3 Clic Test Facility AWAKE Advanced WAKEfield Experiment ISOLDE Isotope Separator OnLine DEvice

LEIR Low Energy Ion Ring LINAC LINear ACcelerator n-ToF Neutrons Time Of Flight HiRadMat High-Radiation to Materials

© CERN2013

Figure 16: CERN's accelerator complex. Source of the figure: [34].

Table 2: Main parameters of LHC [31]

Circumference	27 km
Dipole operating temperature	1.9 K
Number of magnets	9593
Number of main dipoles	1232
Number of main quadrupoles	392
Number of RF cavities	8 per beam
Nominal energy, protons	7 TeV
Nominal energy, lead ions	2.76 TeV per nucleon
Peak magnetic dipole field	8.33 T
Min. distance between bunches	7 m
Design luminosity	$10^{34} \text{ cm}^{-2} \text{ s}^{-1}$
No. of bunches per proton beam	2808
No. of protons per bunch (at start)	1.1×10^{11}
No. of collisions per second	600 millions

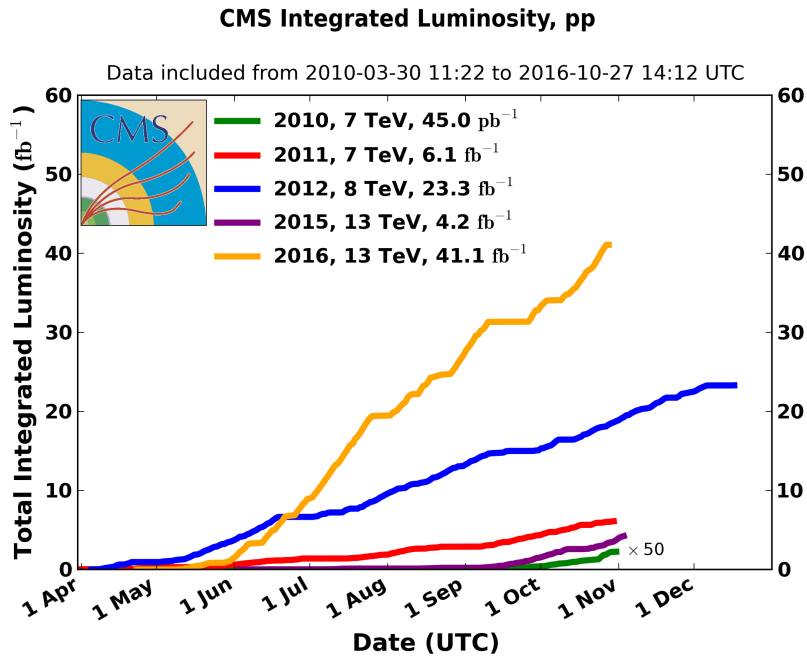


Figure 17: LHC integrated luminosity by year. Source of the figure: [35].

3.2 Compact Muon Solenoid

3.2.1 Introduction

The CMS is a general-purpose detector designed for detecting various highly energetic particles which are being produced in pp collisions at the LHC [38]. The CMS has a broad program with goals of direct and indirect searches of the BSM physics including but not limited to supersymmetric particles. Its main feature is a huge magnet to create a magnetic field of 4T to curve charged particles in the tracking system and of 2T outside to curve muons in the muon system.

The CMS detector is a cylindrically symmetric with a colliding beam as a central axis. Cartesian, cylindrical and spherical coordinates are all used to describe the CMS geometry, depending on the context. The x -axis of the CMS points towards the center of the LHC while the y -axis points vertically up. The direction of the z -axis corresponds to the counterclockwise direction of the LHC beam (Fig. 18, left). Cylindrical coordinates are defined as $r = \sqrt{x^2 + y^2}$, $\phi = \arctan(y/x)$. Instead of the polar angle θ , it is more convenient to use the pseudorapidity $\eta = -\ln \tan \theta/2$. A pseudorapidity ranges from $\eta = -\infty$ to $\eta = +\infty$ for directions parallel to the beam axis with the value of $\eta = 0$ for a direction perpendicular to the beamline. This variable is convenient for measurements because a distribution of a massless particle in η is nearly flat. The acceptance of the CMS in η is limited and varies from $|\eta| < 2.4$ to $|\eta| < 5.0$ depending on a subdetector (Fig. 18, right).

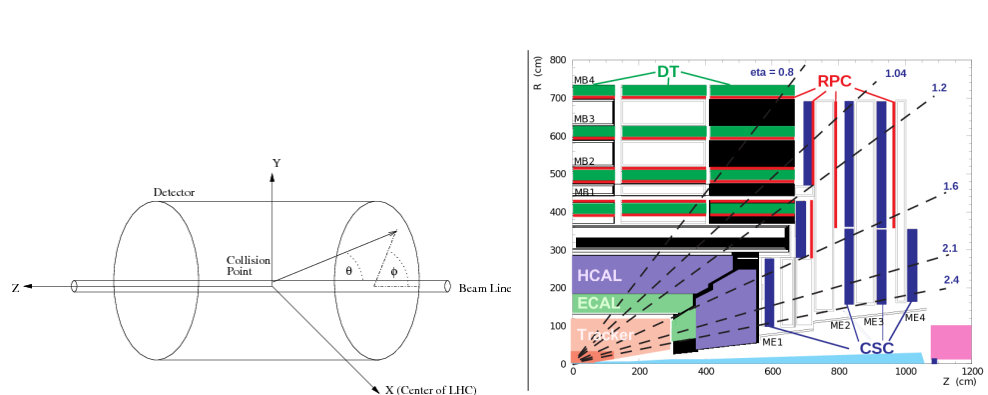


Figure 18: Left: CMS coordinate system. Right: pseudorapidity ranges for different CMS subdetectors.

The detector consists, from inner to outer layer, of a tracking system, an electromagnetic calorimeter (ECal), a hadronic calorimeter (HCal), a magnet and a muon system. Having the tracking system, ECal and HCal inside of a large solenoid makes the detector compact. A segment of a CMS slice in $r - \phi$ plane is shown in Fig. 19.

When a heavy particle is produced in a collision, it decays immediately, and we detect its long-living decay products including an electron, a photon, a muon, a neutral hadron or a charged hadron. Depending on the trace left by a particle in different subdetectors we can identify a particle. Electrons and positrons leave curved tracks in the tracking system and then induce showers in the electromagnetic calorimeter (ECal). Photons induce the same electromagnetic showers in ECal however, as neutral particles, they do not leave tracks in the tracking system. Hadrons normally travel through the ECal undisturbed and induce a hadronic shower in the hadronic calorimeter (HCal). Charged and neutral hadrons can be distinguished from each other by checking whether they leave a track in the tracking system or not. Muons are the only particles which penetrate through the ECal, the HCal and the magnet and leave tracks in the CMS muon system. Neutrinos are not detected by CMS.

844

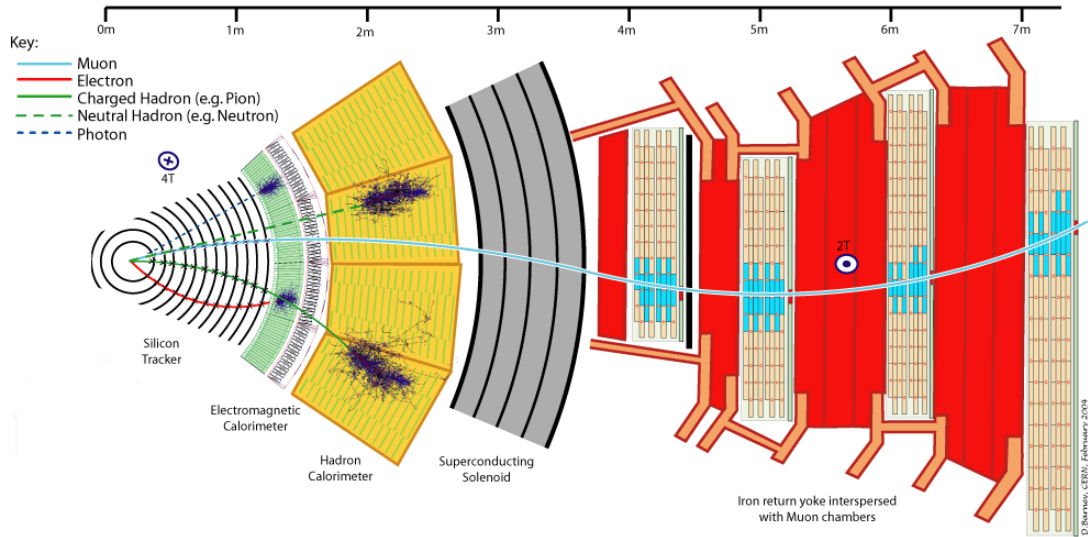


Figure 19: CMS slice.

845 All subdetectors are important for the $W\gamma$ measurement and the remainder of this chapter
 846 describes the subdetectors in greater details. Muons and electrons which we have as final state
 847 particles are both affected by CMS magnetic field allowing the tracking system and the muon
 848 system to measure their trajectory parameters and momenta. In this dissertation we use the
 849 information of the primary vertex determined by the tracking system to select our events. Also
 850 the tracker provide us the information about electrons trajectories and momenta in the electron
 851 channel and distinguishes between electrons and photons. The ECal is necessary to identify elec-
 852 trons and photons and to measure all kinematic parameters of photon. The HCal is also used
 853 for electrons and photons identification: the energy deposit in the HCal left by an electron or a
 854 photon must be very small compared to the energy deposit left in the ECal. The muon system
 855 is essential for muon reconstruction and identification.
 856

857 3.2.2 Magnet

858 A magnetic field in a particle detector is necessary to measure momenta of charged particles by
 859 track curvatures. The higher the momentum is, the less a particle trajectory is affected by the
 860 magnetic field. In CMS a measurement of a charged particle momentum is performed in the
 861 tracking system for all charged particles and in the muon system for muons.
 862

863 The CMS magnet is placed between layers of HCal and a muon system. It creates a magnetic
 864 field of 4T inside the magnet, for the tracking system, and 2T outside the magnet, for the muon
 865 system. It is necessary to have stronger field in the tracking system because a density of tracks
 866 is much higher there than in the muon system and also the tracking system is much smaller and,
 867 therefore, more significant curvature is necessary to measure the momentum with high precision.
 868

869 The magnet is made of superconducting wires. An electric current flowing in the wires creates
 870 a uniform field inside the solenoid and also provides a magnetic field of a certain configuration
 871 outside the solenoid.
 872

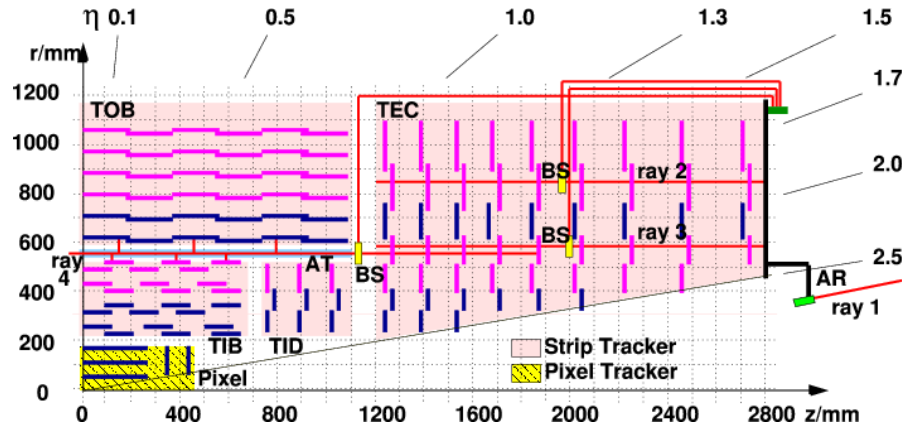
873 3.2.3 Tracking System

874 The tracking system measures track geometry including particles trajectories and locations of
 875 primary and secondary vertices and momenta of charged particles. It needs to disturb particles
 876 as little as possible so that they can pass through. Therefore, just a few measurements must be
 877 enough to reconstruct the track. The accuracy of a measurement of each hit is $10 \mu\text{m}$.

878 The tracking system consists of silicon pixels and silicon strips (Fig. 20). Collision tracks
 879 start at the center and then cross the layers of the tracking system. Tracks are straight in
 880 $r - z$ plane and curved by the magnetic field in the $r - \phi$ plane. The acceptance of the tracker
 881 system in $r - z$ plane is geometrically limited by the absolute value of the pseudorapidity $|\eta| = 2.5$.

884 The pixel tracker is the closest subsystem of CMS to the collision point thus it experiences
 885 the largest particle flux: at 8 cm from the collision point the flux is about 10 million $1/(\text{cm}^2\text{s})$,
 886 and the pixel detector with its 65 millions sensors is capable to reconstruct all these tracks. It
 887 consists of three layers of cylinders in the barrel with radii of 4 cm, 7 cm and 11 cm and four
 888 disks in the endcap, two disks at each side. The tracker is designed in such a way that a single
 889 track hits multiple sensors. Then the trajectory is reconstructed based on how much charge is
 890 collected on each sensor. This allows us to reach a spacial resolution of $15\text{-}20 \mu\text{m}$ which is much
 891 smaller than a distance between sensors.

892 The strip tracker is placed right after the pixel tracker and occupies the detector volume up
 893 to 130 cm around the beam axis. The strip tracker consists of four parts: the tracker inner barrel
 894 (TIB), the tracker inner disks (TID), the tracker outer barrel (TOB) and the tracker endcap
 895 (TEC) as shown in Fig. 20. In the strip tracker there are over 15,000 sensitive modules with a
 896 total number of 10 million strips. Each sensitive module consists of a set of sensors, its support
 897 structure and readout elements.



898 Figure 20: Slice of the CMS tracking system in $r - z$ plane.

900 3.2.4 Electromagnetic Calorimeter

901 The ECal measures energy of electrons and photons and also measures geometries of their
 902 trajectories. Electrons and photons interact with the ECal substance by inducing electromagnetic
 903 showers. Traces left by photons and electrons in the ECal are the same. To distinguish between
 904 these two particles, it is necessary to perform matching to the track in the tracking system. If
 905 there is a track, then there is an electron (or positron). If there is no track, then the particle is
 906 a photon.

908 The ECal is a layer between the tracking system and the HCal. It is made of high-density lead
909 tungstate crystals arranged in a barrel section and two endcap sections. The crystals work as
910 scintillators. When electrons and photons pass through it, it produces light proportional to the
911 particle's energy. The scintillated light then is amplified by photomultipliers producing signals
912 on sensitive elements.

913

914 It is important for the ECal to be able to distinguish between high energetic photons and
915 pairs of lower energetic photons e.g. from a π^0 decay. It is especially difficult in the endcap
916 sections where angle between two photon trajectories is small. ECal preshower located in front
917 of the endcaps which have much smaller granularity provide extra spacial precision. Their strips
918 are 2 mm wide compared to 3 cm wide crystals in the main volume of the ECal.

919

920 **3.2.5 Hadron Calorimeter**

921 The HCal is placed right after the ECal and is the last subdetector within the magnet. The
922 HCal measures energies of charged and neutral hadrons. In addition, the HCal determines the
923 track parameters. Match to the tracking system has to be done: if a matching track found, then
924 it is a charged hadron otherwise it is a neutral hadron.

925

926 The HCal consists of alternate layers of absorbers and scintillators. Hadrons hit brass or steel
927 plate of absorber producing secondary particles. When emerge into the scintillator, the particles
928 induce hadronic and electromagnetic showers and emit blue-violet light which is further shifted
929 to the green region and read out by special boxes within the HCal. The secondary hadrons pro-
930 duced during the interaction with the absorber interact with the next absorber producing more
931 showers in the next layers of scintillators and also affect the total energy deposit. All hadrons
932 must be stopped inside the layers of the HCal.

933

934 **3.2.6 Muon System**

935 Muons pass through the ECal, the HCal and the magnet without interacting. They are the only
936 particles that are registered in the muon system which is placed outside the magnet and which
937 is the largest part of CMS detector.

938

939 There are four concentric layers of muon detectors (stations) and iron return yoke between
940 them. Muons induce several hits in the muon stations which are later fitted and matched to the
941 tracking system measurements to provide the best possible resolution in the measurements of all
942 parameters of the muon's trajectory and momentum.

943

944 There are three types of muon chambers used in the CMS muon system: drift tubes (DTs),
945 cathode strip chambers (CSCs) and resistive plate chambers (RPCs). Overall, there are 1400
946 muon chambers including 250 DTs, 540 CSCs and 610 RPCs.

947

948 The system of DTs measures positions of muons in the barrel. Each DT chamber is about 2 m
949 by 2.5 m in size. It consists of 12 layers of aluminium which are arranged as groups of four. There
950 are up to 60 drift tubes in a layer. The middle group of layers measures z -coordinate and two
951 other groups determine the perpendicular coordinate.

952

953 Each drift tube is 4 cm in width, is filled with a gas and has a wire inside. When a charged
954 particle passes through the volume, it ionizes atoms and the wire receives an electric charge.

955

956 CSCs are placed in endcap regions. CSCs are arrays of anode wires crossed by copper cathode
957 strips placed in a gas volume. When a charged particle penetrates the gas volume, it ionizes the
958 gas. Electrons drift to the wires while ions move to the strips. Strips are perpendicular to wires,

thus, we measure two coordinates for each particle.

RPCs are parallel capacitors made of high-resistivity plastic plates with a space between them filled with a gas. RPCs provide quick measurements of muon momenta and are used for triggering.

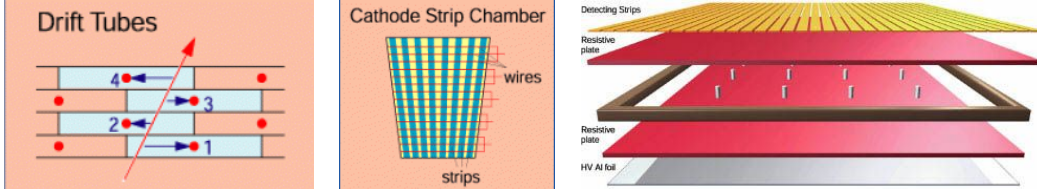


Figure 21: Components of the CMS muon system. Left to right: drift tubes, cathode strip chambers (CSCs), resistive plate chambers (RPCs).

3.2.7 Triggering and Data Aquisition

At peak luminosity, CMS experiences one billion proton-proton collisions per second which come in bunches separated just by 25 ns from one other. New events come before the events from the previous bunch crossing left the detector. To process the information from many different collisions at the same time, data is stored in pipelines.

It is not technically possible to readout all these events. Moreover, we do not need most of these events for a physics analysis because most of these events do not have a potential to discover a new physics. We have resources to store about one hundred events out of one billion that is why we need a trigger system that quickly decides what the best one hundred events are.

If the triggers were too loose, and we would select one hundred events too quickly, e.g., out of a hundred million events, then CMS would not be able to process the rest 90% of events in a given set of one billion and we would lose 90% of potentially interesting events.

If the triggers were too strict, we would select, e.g, ten events out of one billion, not one hundred and lose CMS potential to store and process data by 90% which would significantly reduce our chances for a discovery.

Thus, the challenge of the trigger system is to select the best one hundred events out of one billion and do that fast to be able to process every single event. To achieve this goal, a two-level trigger system was developed consisting from the Level 1 trigger (L1T) and the high level trigger (HLT) as shown in Fig. 22.

L1T is a hardware based trigger (Fig. 23). It uses information from the ECal, HCal and muon system. L1T reduces frequency of coming events from 40 MHz to 100 kHz. Events that did not pass the L1T are lost forever while events that pass the L1T are temporarily stored to get checked by the HLT.

HLT is a software-based trigger. It uses information from all subdetectors and runs quick reconstruction and identification algorithms to determine types of particles and their kinematics. It reduces the number of events to 100 Hz. Events that did not pass HLT are lost forever. Events that pass HLT are arranged into appropriate datasets depending on HLT selection criteria they passed and stored for physics analyses.

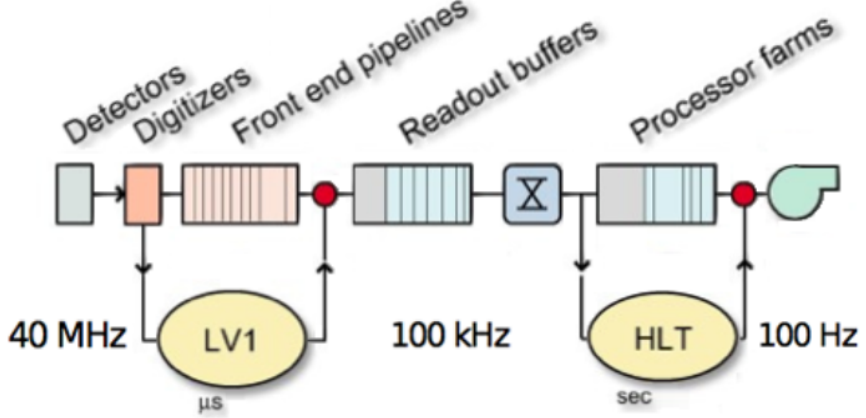


Figure 22: Two-level CMS trigger system.

1000 3.2.8 Particle Flow Algorithm of Event Reconstruction

1001 A particle flow algorithm is used by CMS to identify and reconstruct stable particles [39]. It
 1002 processes the information from all CMS subdetectors and identifies and reconstructs each sta-
 1003 ble particle in an event individually. The list of particles include muons, electrons, photons,
 1004 charged and neutral hadrons. Each type of particles leaves its own trace in CMS subdetectors as
 1005 shown in Fig. 19. After that, jets are built, missing transverse energy E_T^{miss} is determined, certain
 1006 short-lived particles are reconstructed based on the list of individual stable particles in the event.
 1007

1008 One particle can induce several different particle-flow elements in different subdetectors. The
 1009 linking algorithm links these elements together producing blocks of elements. Usually there are
 1010 from one to three elements in each block. Links can be connections between the tracking system
 1011 and silicon strip pre-shower (PS), ECal or HCal, between PS and ECal, between ECal and HCal,
 1012 and between a tracking system and a muon system.
 1013

1014 In each block, muons are considered first. A link between charged tracks in the tracking
 1015 and muon systems comprise a global muon which produces one “particle-flow muon”. The cor-
 1016 responding track in the tracking system is removed from the block and corresponding energy
 1017 deposits are subtracted from ECal and HCal. Then electrons are reconstructed and identifi-
 1018 ed using tracking system and ECal. The corresponding tracks and ECal clusters are removed
 1019 from the block. Remaining tracks and clusters are considered more carefully to identify charged
 1020 hadrons, neutral hadrons, and photons.
 1021

1022 When all particles in the event are reconstructed and identified, E_T^{miss} is determined as

$$E_T^{miss} = - \sum P_T \quad (37)$$

1023 where the summation covers all visible particles in the event. E_T^{miss} is used in physics anal-
 1024 yses as a measure of P_T of neutrinos and other invisible particles in the event. Fake E_T^{miss} can
 1025 originate from particles that did not fall into the detector acceptance, particles with very high
 1026 track curvature that they did not reach the tracking system, momenta mismeasurement, particle
 1027 misidentification, cosmic rays particles, and machine background.
 1028

1029 In the measurement of this dissertation particle flow muons, electrons, photons, and E_T^{miss}
 1030 are used for all the major steps of the cross section measurement including event selection, back-
 1031 ground subtraction, various corrections, and determination of phase space restrictions and bin
 1032 boundaries. Each step is described in greater details in Ch. 5.

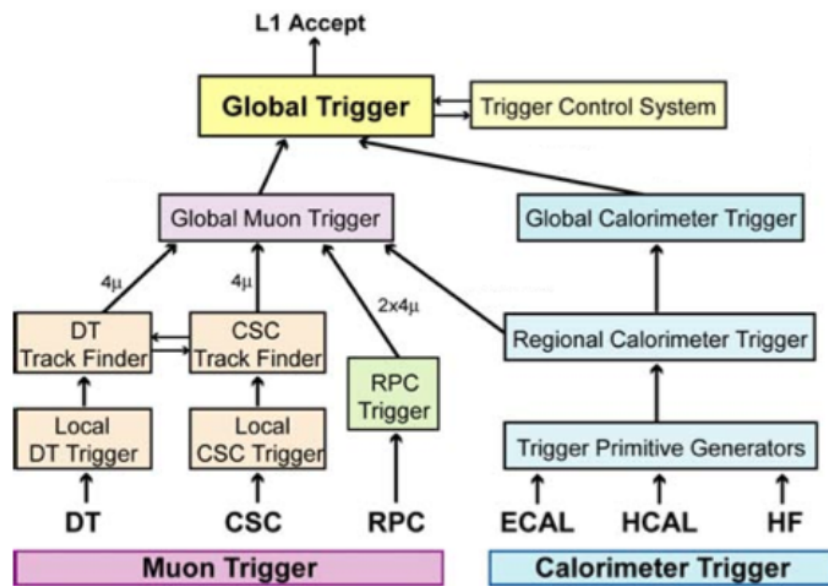


Figure 23: Level 1 CMS trigger system.

1034 4 CMS Tracker Alignment

1035 4.1 Algorithm

1036 Why align?

1037 How to align?

1038 When align?

1039 How to check that your alignment is good?

1040

A tracking system detects hits produced by a charged particle traveling through the detector. In a presence of a constant magnetic field the particle has a helical trajectory. A reconstruction algorithm determines the track parameters by fitting the positions of hits assuming the helix trajectory.

1045

Better hit resolution and the location uncertainty lead to better precision of a measurement of the track parameters. The location uncertainty depends on our knowledge of the positions and orientations in space of the tracking system modules. The hit resolution in the CMS pixel detector is $\sim 15 \mu\text{m}$. When the modules are mounted, their positions are known with precision of $\sim 200 \mu\text{m}$. Thus, we need to know positions of modules 20 times better than they are known when mounted.

1051

The procedure of the determination of the modules locations and orientations is called the tracker alignment. The concept of the track-based alignment can be illustrated in the example of the alignment of a toy tracker. When a charged particle passing through a detector (Fig. 24, top left) it crosses a toy tracker which consists of six flat equidistant modules (Fig. 24, top right). If the modules were placed exactly at their designed positions, we would observe the hits exactly at the points where the track crosses modules at the points of ideal geometry (Fig. 24, middle left). However, in a reality the positions and tilts of the modules are different from ones suggested by the ideal geometry (Fig. 24, middle right). Hits, indeed, are recorded at the places where modules are actually mounted, not at the design ideal places (Fig. 24, bottom left). If we assumed a tracker to be ideal and a track to be smooth, we would see that our hits are off-track (Fig. 24, bottom right). So, we recalculate positions of the modules so that all the hits are laying on the same smooth track (Fig. 25, top left). But these recalculated positions still do not coincide with the actual positions (Fig. 25, top right). Then we record more and more tracks (Fig. 25, middle left and right). We take into account them all and determine the alignment parameters with necessary precision (Fig. 25, bottom left and right).

1066

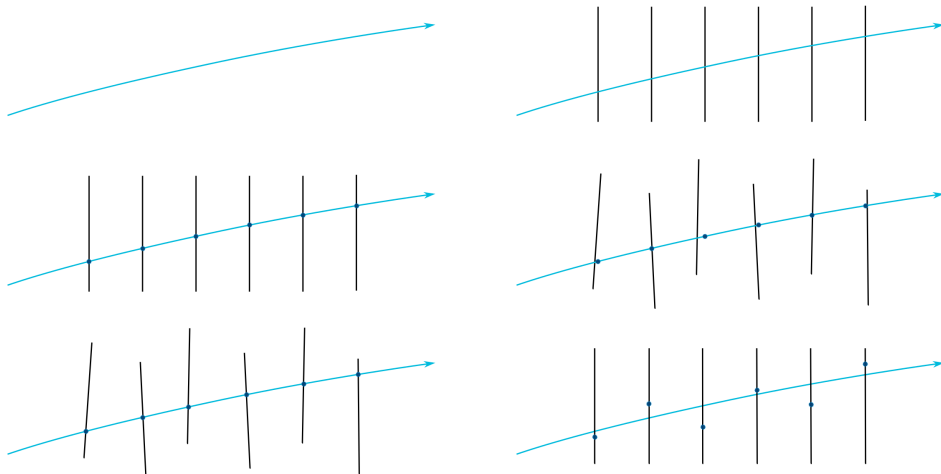


Figure 24: The alignment of a toy tracker, part 1.

1068

When we record a track with a not-aligned tracker, we see that the track is not smooth. But

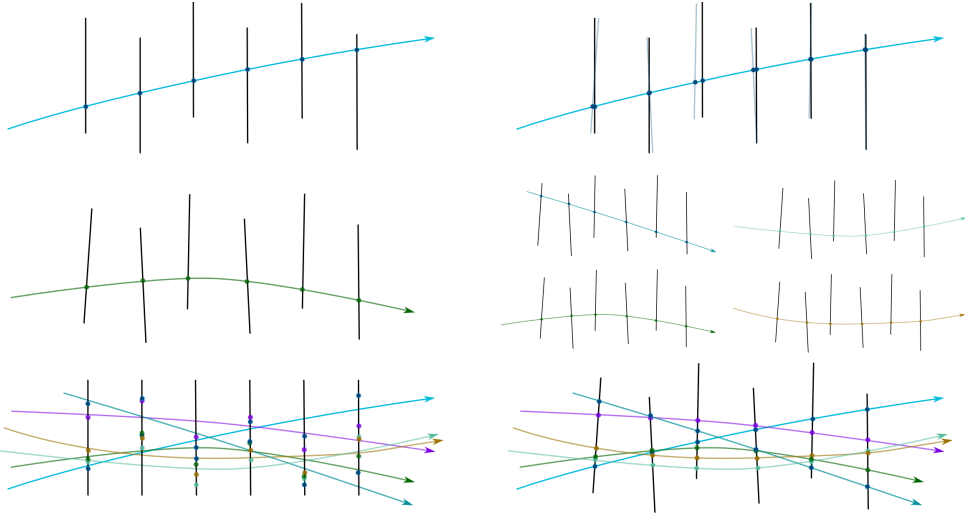


Figure 25: The alignment of a toy tracker, part 2.

that is because our knowledge of module positions is not exact. Thus, we can correct the positions assuming the track is smooth. But when we process the next track, we may find out that the positions have to be corrected again. Thus, we record many tracks and minimize residuals between measured and predicted hits.

The CMS tracker contains 1440 silicon pixel modules in PXB and PXF and 15148 silicon strip modules in TIB, TOB, TID, TEC.

The tracker alignment problem is the least squared problem. The expression to minimize is the following:

$$\chi^2(\mathbf{p}, \mathbf{q}) = \sum_j^{\text{tracks}} \sum_i^{\text{tracks}} \left(\frac{m_{ij} - f_{ij}(\mathbf{p}, \mathbf{q}_j)}{\sigma_{ij}} \right)^2 \quad (38)$$

where \mathbf{p} are parameters describing the tracker geometry, \mathbf{q}_j are parameters of the j^{th} track, $m_{ij} - f_{ij}$ are residuals, distances between the measured hit and a position predicted by the track fit, σ_{ij} is the Gaussian error of the measurement.

We can align the large substructures and individual modules with respect to their substructures. The parameters to align large substructures include their positions and orientations of the subdetectors (rotations). Thus, each subsystem is described by six parameters: three coordinates X, Y, Z and three angles α , β , γ . At the module level, we align positions and rotations with respect to the position s and angles of the corresponding large structure (Fig. 26). In addition, at the module level we align for surface deformations which are described by three parameters per sensor (Fig. 27).

A track can be described with five parameters.

We have two alignment algorithms: Millepede and HIP. Millepede performs a simultaneous fit of all alignment parameters and all track parameters while HIP perform iterative fits of alignment parameters \mathbf{p} and track parameters \mathbf{q}_j .

It is important to use different sorts of tracks for the alignment. Cosmic tracks pass through the detector vertically and do not allow us to connect different subdetectors to one another.

1099 Collision tracks originate from the collision point and go in all directions. However, those tracks
 1100 which cross TEC are all almost collinear and, therefore, it is difficult to measure z -coordinate of
 1101 TEC modules with collision tracks only.

1102

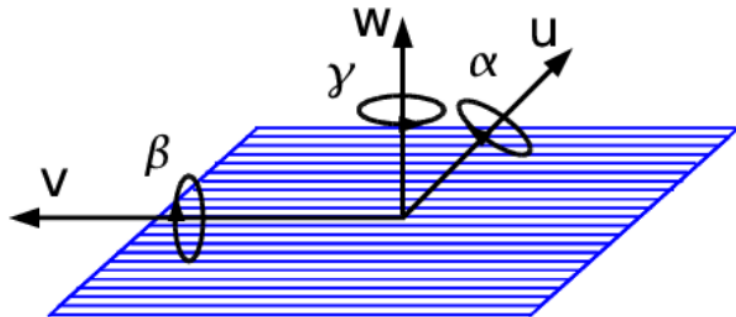


Figure 26: Alignment parameters.

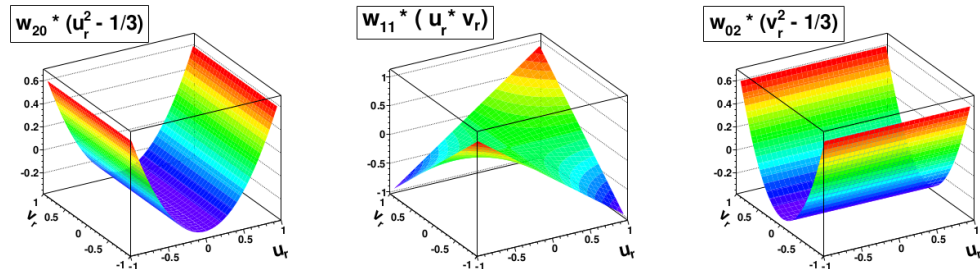


Figure 27: Surface deformations.

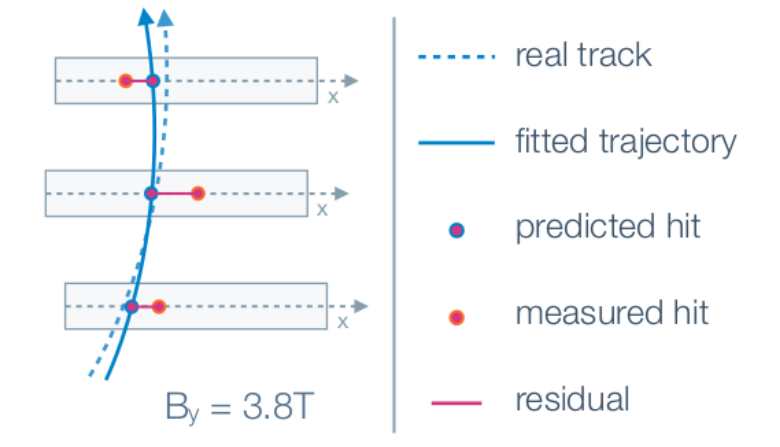


Figure 28: Track residuals.

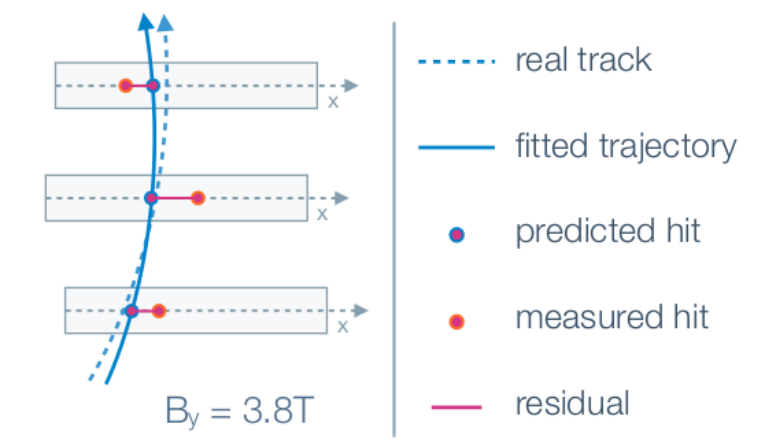


Figure 29: Track residuals.

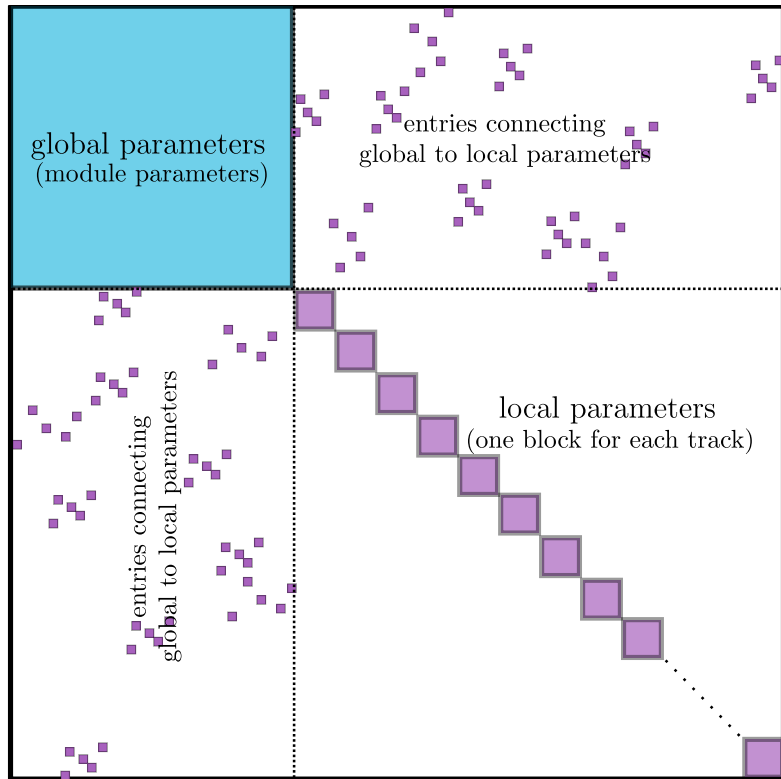


Figure 30: Track residuals.

4.2 Selected Results

1103 CRUZET, CRAFT and first collisions of 2015

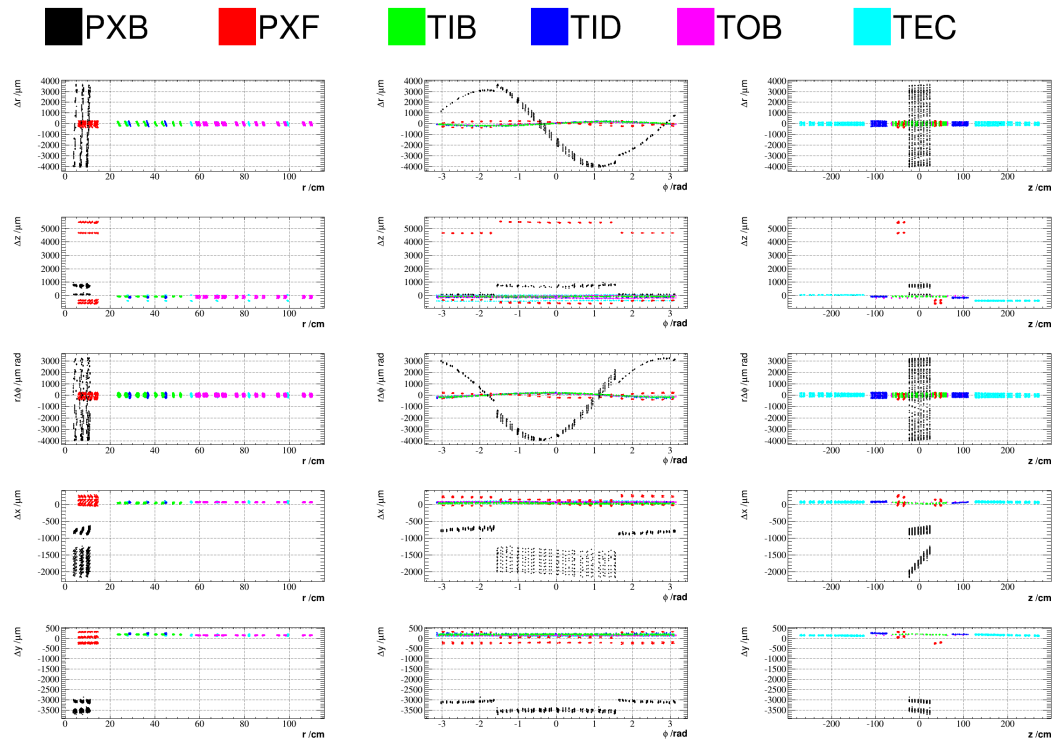


Figure 31: Geometry comparison plot of CRUZET 2015 object vs Run I.

₁₁₀₅ **5 W γ Cross Section Measurement**

₁₁₀₆ Place analysis outline here

1107 References

- 1108 [1] Griffiths textbook
1109 [2] website: <http://www.isgtw.org/spotlight/go-particle-quest-first-cern-hackfest>
1110 [3] CMS Paper about Higgs boson discovery
1111 [4] ATLAS Paper about Higgs boson discovery
1112 [5] PDG
1113 [6] website: <https://science.nasa.gov/astrophysics/focus-areas/what-is-dark-energy>
1114 [7] Pich lectures: The Standard Model of Electroweak interactions
1115 [8] Halzen, Martin "Quarks and leptons"
1116 [9] <http://iopscience.iop.org/article/10.1088/0034-4885/70/1/R02>
1117 [10] Peskin, Schroeder
1118 [11] Lindsey's thesis (CMS Zg- ζ llg, 7 TeV)
1119 [12] website: https://www-d0.fnal.gov/results/publications_talks/thesis/snyder/html/node17.html
1120 [13] website: https://en.wikipedia.org/wiki/Cross_section_%28physics%29
1121 [14] LO (1969) theory paper
1122 [15] NNLO theory paper
1123 [16] NLO theory paper
1124 [17] aTGC paper
1125 [18] Senka's thesis (CMS Wg- ζ munug, 7 TeV)
1126 [19] D0 Combination of $W\gamma$, WW, WZ and VW using 8.6 fb-1 of 2 TeV $p\bar{p}$ collisions Phys.Lett.
1127 B718 (2012) 451-459
1128 [20] LEP Combination of WW and single W using 0.7 fb-1 per experiment of e^+e^- collisions at
1129 WW pair production energies arXiv:1302.3415
1130 [21] 7TeV Wg ATLAS paper
1131 [22] 7TeV Wg CMS paper
1132 [23] ATLAS WW using 20.3 fb-1 of 8 TeV pp collisions Submitted to JHEP
1133 [24] CMS WW using 4.9 fb-1 of 7 TeV pp collisions Eur. Phys. J. C 73 (2013) 2610
1134 [25] CMS WW using 19.4 fb-1 of 8 TeV pp collisions Submitted to EPJC
1135 [26] ATLAS VW ($V=W,Z \rightarrow jj$) using 4.6 fb-1 of 7 TeV pp collisions JHEP 01 (2015) 049
1136 [27] website: https://twiki.cern.ch/twiki/bin/view/CMSPublic/PhysicsResultsSMPaTGC#Figure_1_Limits_on_WW
1137 [28] CMS VW ($V=W,Z \rightarrow jj$) using 5.0 fb-1 of 7 TeV pp collisions Eur.Phys.J. C73 (2013) 2283
1138 [29] CMS 8 TeV WW lnlnmu
1139 [30] CMS 7 TeV Zg nunug
1140 [31]

- 1141 [32] CERN brochure, <http://cds.cern.ch/record/1165534/files/CERN-Brochure-2009-003-Eng.pdf>
- 1142
- 1143 [33] LHC TDR
- 1144 [34] website: <http://home.cern/topics/large-hadron-collider>
- 1145 [35] website: <http://cds.cern.ch/record/1621583/files/>
- 1146 [36] <https://twiki.cern.ch/twiki/bin/view/CMSPublic/LumiPublicResults>
- 1147 [37] website: <http://cds.cern.ch/journal/CERNBulletin/2014/24/News%20Articles/1706606>
- 1148 [38] website: <https://twiki.cern.ch/twiki/bin/view/CMSPublic/LumiPublicResults>
- 1149 [39] CMS TDR
- 1150 [40] paper: <https://inspirehep.net/record/925379/files/PFT-09-001-pas.pdf>